

The geometry of high-dimensional phase diagrams:

II. The duality between closed and open chemical systems

Jiadong Chen¹, Matthew J. Powell-Palm², Wenhao Sun^{1*}

¹Department of Materials Science and Engineering, University of Michigan, Ann Arbor, MI, 48109, USA

²J. Mike Walker '66 Department of Mechanical Engineering, Texas A&M University, College Station, TX, 77802, USA

³Department of Materials Science & Engineering, Texas A&M University, College Station, TX, 77802, USA

*Correspondence to: whsun@umich.edu

Significance Statement

Modern materials are often synthesized or operated in complex chemical environments, where there can be numerous elemental species, competing phases, and reaction pathways. When analyzing reactions using the Gibbs free energy, which has a natural variable of composition, it is often cumbersome to solve for the equilibrium states of a complicated heterogeneous mixture of phases. However, if one is interested only in the stability of a single target material, it may be easier to reframe the boundary conditions around only the target material-of-interest, with boundary conditions open to chemical exchange with an external reservoir. The corresponding phase diagram would thus have a chemical potential axis for the open volatile species, rather than a composition axis. Here we discuss how to derive, compute, and interpret phase diagrams with chemical potential axes, which are dual to the more common composition phase diagram.

Abstract

In our ambition to construct high-dimensional phase diagrams featuring any thermodynamic variable on its axes, here we examine the duality between extensive and intensive conjugate variables in equilibrium thermodynamics. This duality manifests in multiple forms, from the distinction between closed and open boundary conditions of a thermodynamic system, to the relationship between the Internal Energy and its Legendre transformations, to the point-line duality in calculating convex hulls versus half-space intersections. As a representative example, here we derive the duality relationships for chemical work with extensive composition variables, N , and intensive chemical potentials, μ . In particular, we discuss *mixed* composition-chemical potential diagrams, where some species are volatile while others are not; for oxynitride synthesis, lithium-ion cathode stability, and oxide scale formation on compositionally-complex alloys. We further illustrate how chemical potential diagrams directly connect to materials kinetics, revealing the thermodynamic driving forces for non-equilibrium growth and dissolution processes.

Duality is a profound and powerful concept in mathematical physics. As described by Michael Atiyah,¹ duality gives *two different points of view of looking at the same object*. For example, a periodic function can be decomposed into a Fourier series—an infinite sum of sines and cosines; or be represented by its dual the Fourier spectrum—a vector of coefficients for each sine or cosine term. In solid-state physics, Gibbs used duality to invent the concept of the ‘reciprocal lattice’,^{2,3} which is dual to the real-space crystalline lattice—a foundational principle in X-ray diffraction, Bloch wavefunctions, and Ewald summations. A dual representation does not produce any essentially new information, rather, it offers a new perspective to analyze and interpret a physical scenario.

In thermodynamics, there is a duality in how one can ascribe boundary conditions to a thermodynamic system. For a system containing two or more phases coexisting in equilibrium, we can either frame closed boundary conditions around this heterogeneous mixture of equilibrium phases; or if we are interested in the stability of only a single target phase, we could alternatively frame open boundary conditions around only that material, where extensive quantities (heat, volume, mass, *etc.*) are exchangeable with an external reservoir with applied intensive conditions (temperature, pressure, chemical potential, *etc.*). With closed boundary conditions, the relevant phase diagram has the corresponding extensive variable on the axis; whereas for open boundary conditions the relevant phase diagram would have an intensive variable axis. To construct the relevant thermodynamic potential for a phase diagram with natural intensive variables, one uses the Legendre transformation, $\Phi_i = U - \sum_i X_i Y_i$, to change the natural variable of a thermodynamic potential from extensive in $U(X_i)$ to a new potential with the conjugate intensive natural variable, $\Phi(Y_i)$.

Previously in Part I of this three-part series on high-dimensional phase diagrams, we showed that Gibbs’ physical arguments for heterogeneous equilibrium correspond to the lower convex hulls on the Internal Energy surface, $U(S, X_i)$ of the various possible phases. However, due to Gibbs’ stability criterion that $\partial^2 U / \partial X_i^2 > 0$, convex hulls can only calculate heterogeneous equilibrium on thermodynamic axes of extensive variables. In many experimental contexts, the control variables are intensive, like temperature or pressure, which motivates the use of Legendre transformations from $U(S, V, N)$ to the Gibbs free energy $G(T, P, N) = U - (-PV) - TS$. In our ambition to construct generalized high-dimensional phase diagrams with any intensive or extensive thermodynamic variable on the axis, here we discuss the physical interpretation, geometric principles, and computational approaches needed to examine the duality between closed and open thermodynamic systems.

In particular, this work focuses on the duality between closed and open *chemical* systems, where the extensive variable N is mass and the conjugate intensive variable μ is chemical potential. Although chemical potential diagrams have been previously made in the literature,⁴⁻¹³ we believe they are underutilized, which we attribute to a lack of literature that describes how to meaningfully interpret chemical potential diagrams. First, we derive how the duality between convex hulls and half-space intersections offer a computational foundation to connect composition phase diagrams to chemical potential diagrams. We then explore how chemical potential diagrams offer a pathway to connect equilibrium thermodynamics to non-equilibrium materials kinetics—as the equations of diffusion, nucleation, growth, and dissolution, all have terms for chemical potential in their constituent equations.

Finally, we will discuss the limitations of phase diagrams with either all composition axes or all chemical potential axes—as there are many physical scenarios where a system is closed in some elements while being open to others. We advocate for the construction of *mixed* composition-chemical potential phase diagrams, with chemical potential axes for the volatile species and composition axes for the closed species. We examine three case studies of mixed intensive-extensive phase diagrams to interpret the synthesis, operational stability, and growth of: 1) the oxynitride TaON, 2) the lithium-ion battery cathode material LiMn₂O₄, and 3) oxidation of the medium-entropy alloy CrCoNiO_x. To construct these mixed composition-chemical potential diagrams, we combine thermodynamic calculations from both convex hull and half-space intersection algorithms, and discuss the geometry of phase coexistence regions in these mixed diagrams.

More generally, our approach to duality here serves as a general blueprint to Legendre transform the $U(S, X)$ convex hull to any high-dimensional phase diagram, either with axes of all intensive variables (such as elastic stress, electric field, magnetic field, surface area to volume ratio, and others), or some mixture of intensive and extensive variables.

The duality between open and closed thermodynamic systems

It is not meaningful to construct or interpret phase diagrams before establishing the boundary conditions for the thermodynamic system being analyzed. For a material that can undergo chemical reactions, there are two ways to frame boundary conditions, as illustrated in **Figure 1**. When using the Gibbs free energy, which has a natural extensive variable of composition, one frames a *closed* thermodynamic system where the total composition within a reactor is fixed. Inside these closed boundary conditions, an initial non-equilibrium set of reactants will evolve to a final equilibrium phase or a heterogeneous mixture of phases, depending on the ratio of elements in the total reaction vessel. For thermodynamic systems with many phases and chemical species, the resulting network of stoichiometrically-balanced chemical reactions can become very complicated to navigate.¹⁴¹⁵

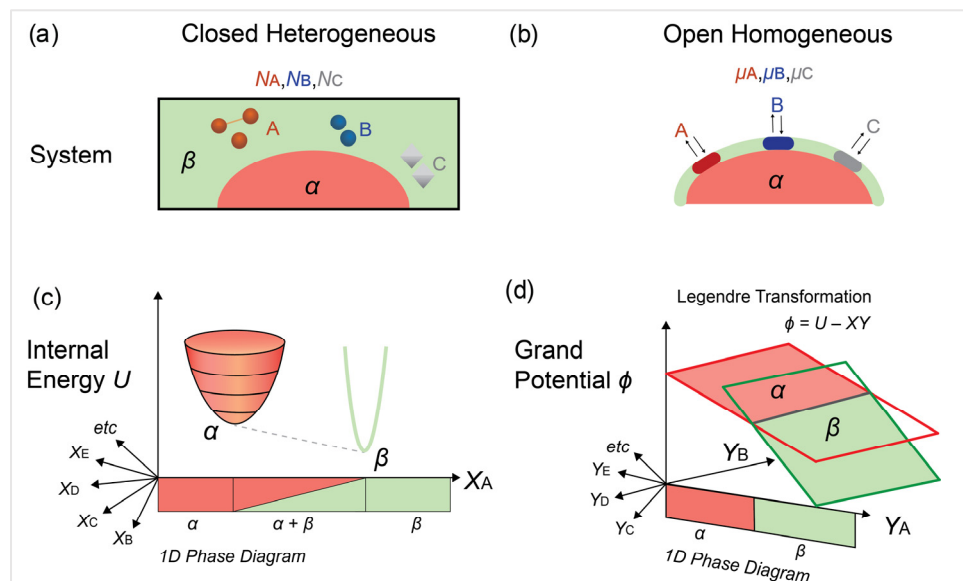


Figure 1. The duality between closed and open thermodynamic systems; shown in (a, b) with corresponding free energy surfaces (c,d), solved with convex hulls on extensive axes, or half-space intersections on intensive axes.

From a materials engineering perspective, our interest may instead only be with regard to a single target phase—for example, to predict optimal synthesis conditions, or to evaluate operational stability in complex chemical environments. In such cases, we may not need to (or care to) fully characterize all the possible reactions within a closed chemical system. Instead, we could frame the thermodynamic boundaries around only the material-of-interest, which we treat as *open* to an external chemical reservoir that has a propensity to deposit mass onto, or dissolve mass away from, our material-of-interest. The thermodynamic propensity to flux mass onto or away from the target material is given by the chemical potential difference between the reservoir and the material.

A few examples where a thermodynamic system might better be described with open instead of closed boundary conditions include the following: In gas-phase deposition, such as chemical vapor deposition or molecular beam epitaxy, one does not usually control the composition of the volatile species; one controls partial pressure, temperature, and flow-rate, which is better described by chemical potential.^{16,17} During precipitation or dissolution from an aqueous electrochemical solution, one usually cares about the material being formed or dissolved, rather than all the various chemical reactions that are possible in H₂O.^{18,19} In heterogeneous solid-state systems, such as the [cathode | electrolyte | anode] system of an all-solid-state battery, one could examine heterogeneous equilibrium in the convex hull isopleth connecting the cathode and anode;¹⁸ or equivalently one could consider the chemical potential differences at the interfaces between the various electrodes in the battery.²⁰ Likewise, one can make similar arguments during solid-state synthesis, as one can examine reactions with composition fixed natural variables,¹³ or equivalently one could examine the chemical potential differences at the interfaces between reactants and products.¹¹

The decision to either model chemical reactions in a closed heterogeneous system, or a collection of subsystems open to each other via chemical exchange, is an arbitrary decision for a human scientist. Nature will evolve the chemical system all the same—but for our conceptual benefit, we should choose our boundary conditions based on whatever considerations are convenient or important to us. To anthropomorphize the target material, it does not ‘know’ the composition of the reaction vessel—it will simply undergo reactions with the chemical reservoir at its physics interfaces. These reactions proceed until the chemical potentials inside the material are equivalent to the chemical potentials with the reservoir at its interface, such that equilibrium is reached.

The duality between convex hulls and half-space intersections

Chemical potential diagrams have previously been calculated, most notably by Yokokawa⁴, and have been applied to study solid-oxide fuel cells,⁵ hydrogen storage materials,⁶ surface adsorption,^{7,8,9} defects,^{9,11} and materials synthesis.^{11,13} In our overarching ambition to calculate high-dimensional phase diagrams, it is important to use computational phase diagram approaches that are scalable to many dimensions. Published algorithms for computing chemical potential diagrams, from our perspective, rely on inelegant approaches, often involving for loops or inefficient optimization approaches, and do not scale well to high-component chemical spaces. In addition, published chemical potential diagrams only depict equilibrium situations, while here we derive chemical potential diagrams that can represent non-equilibrium scenarios like crystal growth and dissolution.

Our derivation of the chemical potential diagram below is inspired by the discussions in Callen²¹, Zia²², and Yokokawa⁴, but it is derived in a way specifically to leverage the duality between convex hulls and half-space intersections, which are computational optimization algorithms that readily scale to higher dimensions. First, we will connect the Legendre transformation to Point-Line Duality. Then we will use Point-Line Duality to connect convex hulls to half-space intersections. From our perspective, these ideas appear in the literature in scattered form, which our goal here is to unify under one physical, mathematical and computational perspective. For the sake of completeness, we present a full derivation in the **SI1-SI3**. A brief summary of the derivation follows:

For phase diagrams with extensive variables, the equilibrium state is solved by convex hulls, and each state of a phase is given by a vertex on the convex hull. We then leverage a concept from projective geometry named *Point-Line Duality*. Briefly summarized: for a line of the form $y = ax - b$, it is usually customary to treat x and y as the axes, and a and b as parameters for the line. However, since a and b provide all the information needed to define this line, we could equivalently represent this line as a point (a, b) in $a-b$ space. Symmetrically, one can swap a, b and x, y to arrive at a similar relationship between lines in $a-b$ space and points in $x-y$ space. If the line is provided as an inequality, $y \leq ax - b$, one can show that the lower convex hull for a collection of points is equivalent to the lower half-space intersection for its dual representation of lines.

In mathematics, the Legendre transformation is a method to relate a convex function to its envelope of tangent lines. Because the tangent line to a $U(X_i)$ surface, $\partial U / \partial X_i$, gives the intensive variable Y_i ; the Legendre transformation is a natural implementation of Point-Line duality. For a natural intensive variable of chemical potential, the Legendre transformation can be used to construct a new thermodynamic grand potential, $\phi = G - \mu N$. For composition axes, it is customary to transform the number of mols, N , to mol fraction, x , by the affine relationship $\sum x_i = 1$, where $x_i = N_i / \sum_i N_i$. This changes the intensive variable μ from the slope $\partial G / \partial N$, to the intercept rule (derivation in **SI3.2**), where $\mu_i = G - (1-x_i) \cdot [dG/dx_i]$. Graphically, μ_i can be solved by a tangent line of the convex hull, extended to the vertical G axis at the elemental end-point compositions, as later illustrated in **Figure 2a**. Hence, the chemical potential denoted as μ in this context represents the relative chemical potential to a standard reference state. In some published papers, it is expressed as $\Delta\mu(\mu - \mu^0)$.

The $\phi(\mu)$ space is dual to the $G(x)$ space. Each phase, which was a vertex in $G(x)$ space, becomes a line in the dual $\phi(\mu)$ space. More generally, in higher dimensions, each phase becomes a hyperplane by the equation $\phi = G - \sum \mu_i x_i$, which corresponds directly to $y = \sum a_i x_i - b$. The equilibrium state in $G(x)$ was solved using a bounding lower-convex hull of vertices, which in dual $\phi(\mu)$ space, corresponds to a bounding upper half-space intersection of hyperplanes. A mathematical proof of this duality is provided in **SI2**.

Phase diagrams are constructed by projecting the lowest free-energy phases onto the thermodynamic axes, thus eliminating the energy axis. For example, a T - P phase diagram is constructed by projecting the half space intersection of $G = H + PV - TS$ onto the T and P axes. Likewise, a composition phase diagram is a projection of the $G(x)$ convex hull onto the composition axes; and a chemical potential diagram is a projection of the lower half-space envelope of ϕ surfaces onto chemical potential axes (**Figure 2b**). The stability region of a phase on a chemical potential diagram shows chemical potential values where its grand potential is lower than that of any other phase.

Table 1. Dual representation of physical aspects in closed system (the convex hull) and open system (chemical potential diagram).

Physical Aspects		Dual Representation	
System	Boundary Condition	Closed to mass transfer	Open to mass transfer
Thermodynamic Aspects	Thermodynamic Potential	Gibbs potential	Grand potential
	Euler form	$G = U + PV - TS$	$\Phi = G - \mu N$
	Differential Form	$dG = -SdT + vdP + \mu dN$	$d\Phi = -SdT + vdP - Nd\mu$
	Natural Variables	T, P, N	T, P, μ
	Heterogeneous Equilibrium	Coexistence region	Phase boundary
	Metastability	Energy above the hull	Growth
	Instability	Decomposition energy	Dissolution
Geometric aspects	Phase	Point	Hyperplane
	Equilibrium state	Convex Hull	Half-space intersection

In this work, we will present chemical potential diagrams for a variety of systems. All the thermochemical data for these diagrams are from the Materials Project database²³, which is a database of high-throughput DFT-calculated enthalpies of ordered crystalline phases. As is common in the computational materials science community, we assume that vibrational entropy is negligible in solids, so that we can approximate $G_{\text{solid}} = E_{\text{Solid,DFT}}$ ²⁴. The Materials Project only contains ordered crystalline phases, so we do not consider the solid-solution phases, although they are certainly relevant in real materials. Finally, DFT has known errors in formation energy^{25,26}, but the Materials Project has implemented a series of energetic corrections^{27,28,29} which we adopt here without further scrutiny. For a thorough analysis of the actual chemical systems presented here, it would be appropriate to recalculate the thermochemical data without these assumptions—however this work primarily emphasizes the formalism, geometry and interpretation of chemical potential diagrams, so we use the unaltered Materials Project data for our visualizations.

Equilibrium and non-equilibrium regions on a chemical potential diagram

When analyzing the stability of a material under open boundary conditions, one should distinguish in the mind between the *internal* intensive variable of a substance, Y_i , versus the *external* intensive variable of the reservoir Y_{external} . If the $Y_{\text{internal}} \neq Y_{\text{external}}$, then the conjugate extensive quantity X will flow through the boundary until $Y_{\text{internal}} = Y_{\text{external}}$, after which entropy will be maximized and equilibrium is reached. For example, if 50°C water is exposed to an external temperature reservoir of 10°C, heat will flow out of water into the reservoir, and the entropy of water will be reduced correspondingly. Water has a continuous span of entropies in this temperature range, so it can change its *internal* extensive entropic state to equilibrate with an *external* intensive temperature reservoir.

Likewise, for chemical work, to equilibrate the internal chemical potential of a material with the external chemical potential of the reservoir, mass can be transferred across the boundaries. At **equilibrium**, the externally applied chemical potential reservoir will be exactly equal to the internal chemical potential of a material; $\mu_{\text{material}} = \mu_{\text{reservoir}}$, such that there is no driving force to transfer mass to or from the reservoir. For a **non-equilibrium** situation, if external chemical potentials are different than the internal chemical potentials of a material, mass will have a propensity to flux from high μ to low μ ; where a material will grow if $\mu_{\text{reservoir}} > \mu_{\text{material}}$, or it will dissolve or corrode if $\mu_{\text{reservoir}} < \mu_{\text{material}}$. Because growth and dissolution are fundamental aspects of materials kinetics, chemical potential diagrams offer a direct link between non-equilibrium thermodynamics and kinetics of transport.

The internal chemical potential of the material derives from the energies of its quantum-chemical and electrostatic bonds—which determines its scalar formation energy. **Figure 2a** visualizes the formation energies of phases from the Mn-O system with its interpretation for equilibrium and non-equilibrium scenarios from the perspective of a convex hull. The corresponding chemical potentials can be interpreted from the intercept rule—where μ_{Mn} or μ_{O} are the intercept of the tangent lines of the convex hull with the vertical energy axis at the elemental end-point compositions.

The **equilibrium** chemical potential window of the single phase Mn_3O_4 is bound between the cotangent lines of $\text{Mn}_2\text{O}_3/\text{Mn}_3\text{O}_4$ and $\text{Mn}_3\text{O}_4/\text{MnO}$, where these cotangent lines indicate the chemical potentials where Mn_3O_4 can coexist in equilibrium with Mn_2O_3 or Mn_3O_4 . **Figure 2b** shows the corresponding chemical potential windows of each Mn_xO_y phase, indicated by the vertical line segments at a given composition. Because phases on the convex hull are points, the Legendre transformation of these phases form the grand potential surfaces, whose half-space intersection is shown **Figure 2d**. The condition where the *externally* applied chemical potentials are equal to the *internal* chemical potential of a material can be written as:

$$\phi = [G]_{\text{internal}} - [\sum_i \mu_i x_i]_{\text{external}} = 0.$$

Therefore, the conditions of equilibrium on a chemical potential diagram correspond to a *slice* of grand potential surfaces where $\bar{\phi} = 0$, accentuated by the darker lines on **Figure 2d**. We call this the *equilibrium envelope* of the chemical potential diagram. All regions in chemical potential diagrams display the external chemical potential applied by the reservoir, but darker lines additionally represent the situation where *internal* chemical potential of each material on the convex hull is equal to the external chemical potential from the reservoir. The lines formed by the equilibrium envelope ($\phi = 0$) are consistent with the vertical segments formed by intercept rule as illustrated in **Figure 2b**.

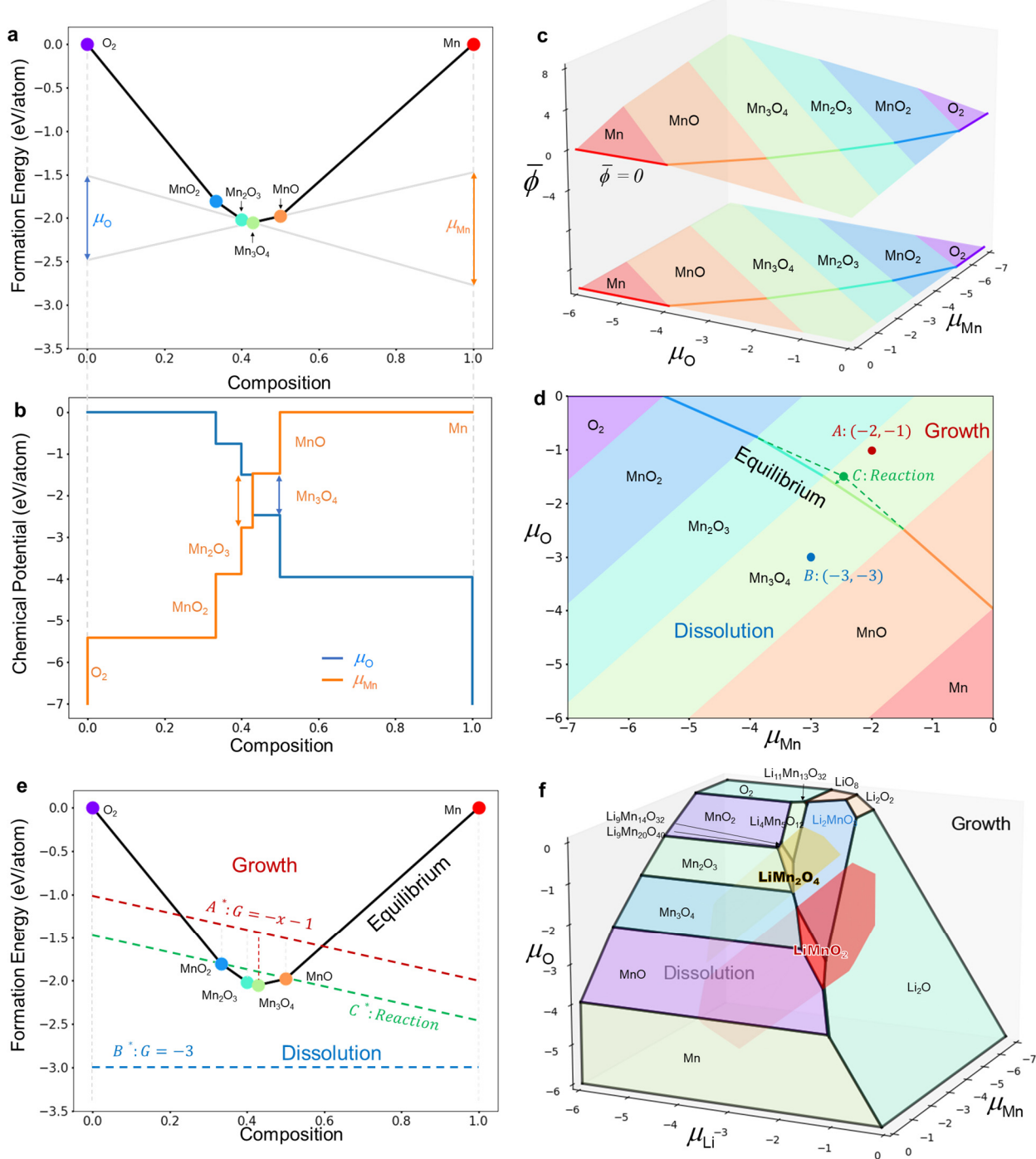


Figure 2. Duality between convex hulls and chemical potential diagrams in the binary Mn-O system. (a) Tangent lines to the convex hull, and their intercepts with the energy axes, show the elemental chemical potential window for Mn_3O_4 . (b) Chemical potential windows for μ_{Mn} and μ_{O} various MnO_x phases indicated by vertical segments. (c) Grand potential hyperplanes for the Mn-O chemical potential diagram. The equilibrium envelope is emphasized by a dark line at $\phi = 0$ (d) Dissolution and growth regimes on the chemical potential diagram and (e) their dual relationship with the convex hull. (f) Ternary chemical potential diagram, with the growth and dissolution regimes for LiMn_2O_4 and LiMnO_2 illustrated as extending in and out of the stability regions on the equilibrium envelope.

The equilibrium envelope further separates a chemical potential diagram into non-equilibrium regions of growth and dissolution. For example suppose Mn_3O_4 is placed in contact with an external chemical reservoir where the boundary conditions are $(\mu_{\text{Mn}}, \mu_{\text{O}})_{\text{external}} = (-2, -1)$, indicated by the red label **A** in **Figure 2d**. These chemical potentials are higher than the internal μ_{Mn} and μ_{O} in Mn_3O_4 , so Mn and O will flux from the external chemical reservoir onto Mn_3O_4 , leading to crystal growth. On the convex hull in **Figure 2e**, the dual representation to this point on the chemical potential diagram corresponds to the line **A*** on the convex hull. Likewise, if Mn_3O_4 is exposed to low $(\mu_{\text{Mn}}, \mu_{\text{O}})_{\text{external}} = (-3, -3)$, shown as point **B** in **Figure 2d** and the line **B*** in **Figure 2e**, Mn and O will flux out of Mn_3O_4 into the reservoir, leading to dissolution of Mn_3O_4 . The precise chemical or structural nature of the external chemical reservoirs are irrelevant, only their μ_{Mn} and μ_{O} chemical potentials matter.

The chemical potential diagram can also show conditions for solid-solid phase transformation from a metastable solid to an equilibrium phase. If a different MnO_x phase, for example Mn_2O_3 , were exposed to an external chemical potential such as point **A** or **B**, which is in the non-equilibrium region corresponding to Mn_3O_4 , there would first be a thermodynamic driving force for phase transformation from Mn_2O_3 to Mn_3O_4 , followed by subsequent growth or dissolution of Mn_3O_4 . In the convex hull of **Figure 2e**, the phase transformation that originates from Mn_3O_4 has the largest energy drop from line **A*** compared to all other MnO_x phases. Nucleation and diffusion kinetics aside, the bulk driving force prefers the transformation and further growth of Mn_3O_4 . Additionally, because Mn_3O_4 has the shallowest energy drop to **B***, any other MnO_x composition exposed to this external chemical reservoir can first reduce its free energy by transforming to Mn_3O_4 , and then dissolving mass out to the reservoir.

Additionally, chemical potential diagrams can be employed to illustrate solid-state reactions. In **Figure 2e**, the green dashed line, denoted as **C***, represents the reaction between MnO_2 and MnO . By Point-Line duality, this corresponds to point **C** in the chemical potential diagram (**Figure 2d**), which is the intersect between the extension of the equilibrium envelope lines for MnO_2 and MnO . The reaction driving force is the distance from point **C** to the Mn_3O_4 equilibrium envelope along the $\mu_{\text{O}}: \mu_{\text{Mn}} = 1$ direction. This reaction energy on the chemical potential diagram is equal to the distance between **C*** and Mn_3O_4 on the convex hull.

Our geometric interpretation of the binary convex hull and chemical potential diagram can be readily extended to higher component systems. **Figure 2f** illustrates a ternary $\mu_{\text{Li}}\text{-}\mu_{\text{Mn}}\text{-}\mu_{\text{O}}$ chemical potential diagram. The chemical potential diagram exists in 3 dimensions, since one can vary all three chemical potentials independently for non-equilibrium scenarios. However, the equilibrium envelope is still a 2-dimensional manifold, due to the special constraint that $\bar{\phi} = [G]_{\text{internal}} - [\sum_i x_i \mu_i]_{\text{external}} = 0$. Nonetheless, one can see that the non-equilibrium regions similarly extend into and out of the equilibrium manifold, for example as highlighted for LiMn_2O_4 (yellow) and LiMnO_2 (red). All other arguments of growth and dissolution can be applied to this ternary chemical potential diagram.

Mixed Composition-Chemical Potential Diagrams

There are many physical situations where a chemical system is open to some elements, but are closed in others. For example, in the stability of metal oxynitrides, oxygen and nitrogen can be volatile, whereas the metal(s) usually are not. In such cases, pure chemical potential diagrams or pure compositional phase diagrams may not be the most useful. Here we advocate for the construction of mixed composition and chemical potential phase diagrams, interpreting three representative case studies for oxynitride stability, lithium-ion cathode stability, and oxidation of multicomponent alloys.

Although mixed composition-chemical potential diagrams can be interpreted from the geometry of the intercept rule, they are not straightforward to calculate, as they require using convex hulls in the composition axes, and then half-space intersections for the chemical potential axes. We present a method where equilibrium is calculated both with convex hulls and half-space intersections, then the coordinates of each phase are mixed-and-matched depending on if the desired axis is composition or chemical potential. Details of this computational implementation are discussed in **SI4**.

Metal oxynitrides

Oxynitrides are a class of mixed-anion materials with applications for semiconductors and optoelectronics,³⁰ water-reduction photocatalysts,³¹ electrocatalytic nitrogen reduction,³² hard coating,³³ energy storage,^{34,35} etc. Introducing additional anions with different sizes, electronegativities, and charges can effectively modulate the physical properties of oxide-based compounds^{36,37}. However, oxynitrides are difficult to synthesize, and if synthesized, do not always retain operational stability (for example during catalysis in harsh electrochemical environments). Here, we examine the boundary conditions and relevant phase diagram in evaluating the stability of tantalum oxynitride, TaON.

It is not straightforward to experimentally control the oxygen and nitrogen *composition* in a reaction vessel, as oxygen and nitrogen are gases at standard state and at elevated temperatures. For this reason, it is not very convenient to examine oxynitride stability on phase diagrams with oxygen and nitrogen *composition* axes. If we are only concerned about the stability of the oxynitride, we can instead frame our thermodynamic system around just the oxynitride itself, with boundary conditions open to oxygen and nitrogen transfer, while closed in the non-volatile metal species. The corresponding phase diagram should therefore be a mixed $x_{\text{metal}}-\mu_{\text{O}}-\mu_{\text{N}}$ diagram.

In **Figure 3a**, we illustrate the geometric connection between an all-extensive $x_{\text{metal}}-x_{\text{O}}-x_{\text{N}}$ convex hull with its mixed $x_{\text{metal}}-\mu_{\text{O}}-\mu_{\text{N}}$ phase diagram. For a target TaON phase, the blue triangle indicates the tangent plane to the TaON vertex. The intercept of this tangent plane with the energy axes at the pure elemental compositions corresponds to the elemental chemical potentials. Tilting this tangent plane about the TaON vertex maps out μ_{O} and μ_{N} chemical potentials where TaON is a stable equilibrium phase. This tangent plane tilting process is similar to retrieving the temperature and pressure of a phase on the Maxwell *U-S-V* surface, except that on the Maxwell surface the slope of the tangent plane $\partial U/\partial X$ directly gives the intensive variable *Y*, whereas in affine composition axes (where $x_1 = 1 - x_2 - x_3$), the conjugate intensive chemical potential variable is given by the intercept rule.

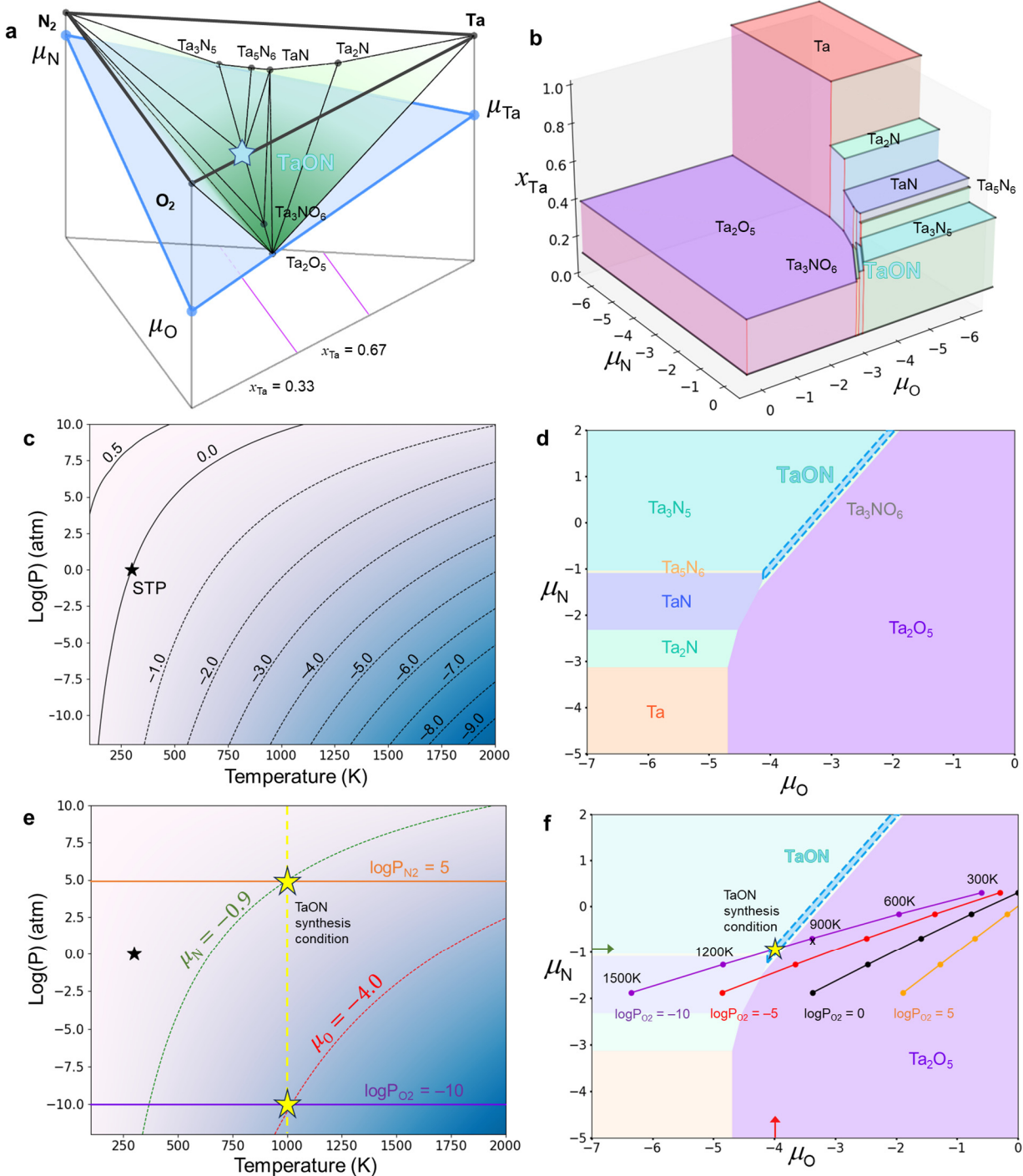


Figure 3. **a)** Ternary $x_{\text{Ta}}\text{-}x_{\text{N}}\text{-}x_{\text{O}}$ convex hull. Blue triangle represents tangent plane to the TaON vertex, whose intercepts with the energy axis provides the corresponding elemental chemical potentials. **b)** Mixed $x_{\text{Ta}}\text{-}\mu_{\text{O}}\text{-}\mu_{\text{N}}$ phase diagram. **c)** The chemical potential of a diatomic gas like O_2 or N_2 , as a function of temperature and partial pressure. Iso- μ lines are marked from -9 to 0.5 eV/atom. **d)** $\mu_{\text{O}}\text{-}\mu_{\text{N}}$ projection of the mixed $x_{\text{Ta}}\text{-}\mu_{\text{O}}\text{-}\mu_{\text{N}}$ diagram. **e)** Gas conditions for N_2 and O_2 where TaON is stable, marked with yellow star. **f)** Lines on the $\mu_{\text{O}}\text{-}\mu_{\text{N}}$ projected diagram corresponding to gases at various partial pressures, where we fixed $\log P_{\text{N}_2} = 5$, and then show isolines corresponding to μ_{O} and μ_{N} at various $\log P_{\text{O}_2}$ and temperature.

The $x_{\text{Ta}}-\mu_{\text{O}}-\mu_{\text{N}}$ phase diagram is shown in **Figure 3b**, where single-phase regions correspond to horizontal polygons with black borders parallel to the μ_{O} and μ_{N} axis. 2-phase coexistence regions are formed by the vertical rectangles connecting two single-phase polygons parallel to the x_{Ta} direction. The 3-phase coexistence regions are given by the vertical red lines that connect two 2-phase coexistence regions. The x_{Ta} axis shows how changing μ_{O} and μ_{N} can control the Ta molar fraction. However, this 3-dimensional diagram can also be projected onto just the $\mu_{\text{O}}-\mu_{\text{N}}$ axes, as in **Figure 3d**.

The chemical potential of a gaseous phase is given by $\mu_{\text{gas}} = \mu_{\text{O}} + RT\ln[P_{\text{gas}}] - TS_{\text{gas}}$, where μ_{O} is the standard state chemical potential, P_{gas} is the partial pressure, and S_{gas} is its entropy. $\text{N}_2(\text{g})$ and $\text{O}_2(\text{g})$ are the equilibrium elemental phases at standard state, so for both oxygen and nitrogen, $\mu_{\text{O}} = 0$ at 298K and $P = 1$ atm. The dependence of μ_{gas} on temperature and partial pressure is schematized in **Figure 3c**, which provides an experimental reference guide that can be used together with the $x_{\text{Ta}}-\mu_{\text{O}}-\mu_{\text{N}}$. The combination of **Figures 3b, c, d** provides theoretical utility similar to the Ellingham diagram, however the Ellingham diagram cannot examine materials stability with two independent volatile gaseous species, whereas the chemical potential diagram construction can.

Although TaON is on the $\text{Ta}-\text{O}-\text{N}$ convex hull, and is therefore a thermodynamically stable phase, its stability window is very narrow in the $\mu_{\text{O}}-\mu_{\text{N}}$ diagram, meaning that the conditions to stabilize TaON may need to be very precise. In particular, μ_{N} should be much greater than μ_{O} for TaON to be stable. In **Figure 3f**, we place a yellow star in the TaON stability window at $(\mu_{\text{O}}, \mu_{\text{N}}) = (-4 \text{ eV}, -0.9 \text{ eV})$. By referencing the diagram in **Figure 3e**, we can determine the O_2 and N_2 gas conditions that correspond to this TaON stability point.

For an oxynitride exposed $\text{O}_2(\text{g})$ and $\text{N}_2(\text{g})$, the temperatures of the two gases will be the same—however, their relative partial pressures can be varied independently. On **Figure 3e**, we should search for a temperature (a vertical line) that intersects iso- μ lines of -0.9 eV for N_2 , and -4 eV for O_2 . One such condition is at 1000K, with $\log P_{\text{N}_2} = 5$ and $\log P_{\text{O}_2} = -10$. In **Figure 3f**, we use a series of dotted lines to represent different temperatures and different $\log P_{\text{O}_2}$, with each line having a fixed $\log P_{\text{N}_2} = 5$. For most conditions, these lines fall in Ta_2O_5 region, showing that TaON is unstable with respect to Ta_2O_5 under most conditions in air. However, for the line $\log P_{\text{O}_2} = -10$, we can intersect the TaON region at 1000K.

Although we conducted our stability analyses with respect to O_2 and N_2 gas, we can use other nitrogen or oxygen precursors to shift the μ_{N} and μ_{O} chemical potentials. For example, to overcome the triple bond in the N_2 molecule, nitrides are usually much more readily synthesized with activated nitrogen precursors, such as ammonia where the half reaction $\mu_{\text{N}} = \mu_{\text{NH}_3} - 3/2 \mu_{\text{H}_2}$ yields $\mu_{\text{N}} = 0.4 \text{ eV}$ at standard state; and plasma-cracked atomic nitrogen has been benchmarked to $\mu_{\text{N}} = 1 \text{ eV/N}$.^{38,39} These chemical potentials are equivalent to $\text{N}_2(\text{g})$ partial pressures of 10^{16} atm and 10^{40} atm , respectively. A low oxygen chemical potential can also be obtained by reducing agents, for example, reduction with carbon monoxide yields an equilibrium chemical potential of $\mu_{\text{O}} = \mu_{\text{CO}_2} - \mu_{\text{CO}} = -2.6 \text{ eV/atom}$ at STP, equivalent to an $\text{O}_2(\text{g})$ partial pressure of 10^{-104} atm (assuming the reaction is not kinetically-limited). Similar analyses can be done to obtain the effective chemical potential of chemical species in various other states, including solvated aqueous ions, or atoms in other solids.

The $x_{\text{Ta}}-\mu_{\text{O}}-\mu_{\text{N}}$ chemical potential diagram can also yield other insights that cannot be readily obtained from a compositional phase diagram. **Figure 3d** show that to reduce Ta_2O_5 to metallic Ta, μ_{O} needs to be below -4.6 eV, which are also conditions generally needed to synthesize pure tantalum nitrides. The phase boundary between the various tantalum nitrides TaN_x and the Ta_2O_5 also indicates conditions for the stability of the pure tantalum nitrides in air.

Stability of the Li-ion cathode material LiMn_2O_4

LiMn_2O_4 is a candidate cathode material for rechargeable Li-ion batteries, in particular because Mn is not a critical element like cobalt-based battery electrodes.^{40,41} LiMn_2O_4 has a spinel crystal structure with diffusion channels that enable fast diffusion of Li^+ , even at relatively low concentration of Li^+ .^{42,43} However, during the synthesis and electrochemical operation of LiMn_2O_4 , many competing ternary $\text{Li}_x\text{Mn}_y\text{O}_z$ phases can form, such as $\text{Li}_4\text{Mn}_5\text{O}_{12}$ and LiMnO_2 , as well as the solid-solution phases that can form between these ternary phases and MnO_2 , Mn_3O_4 . (**Figure 4a,b**). The complexity of the available phases and structural transformations, especially between layered rocksalt structures and the spinel structures, can result in undesired phases in the form of impurities during synthesis, as well as irreversible decomposition pathways during electrochemical cycling and operation.

Under various synthesis or operation contexts, all 3 elements Li, Mn and O can be volatile in LiMn_2O_4 . The oxygen chemical potential can be controlled by an oxidizing or reducing environment during synthesis, and likewise thermal decomposition by metal reduction and oxygen evolution also depends on μ_{O} .⁴⁴ During battery charging and discharging, Li is cycled in and out of LiMn_2O_4 through the electrolyte,²⁰ where $\mu_{\text{Li}} = \mu_{\text{Li,metal}}^0 - e\varphi$,¹⁸ where φ is the electric potential, and $\mu_{\text{Li,metal}}^0 = 0$ because μ is referenced to the chemical potential to elemental Li. Because the electrolyte is adjacent to LiMn_2O_4 , the electrolyte can exchange Li, Mn or O with LiMn_2O_4 . In particular, one major issue hampering the widespread adoption of manganese-based cathodes is dissolution of the redox-active Mn ion in organic electrolytes, where Mn diffuses through the electrolyte to form an undesirable solid-electrolyte interface (SEI) at the anode, which erodes overall battery capacity.⁴⁵

Although all three elements can be exchanged through an open boundary condition, it can be confusing to analyze LiMn_2O_4 stability on a full $\mu_{\text{Li}}-\mu_{\text{Mn}}-\mu_{\text{O}}$ chemical potential diagram, since it becomes difficult to isolate the work of the reservoir on the individual volatile species. It may be better to close the system to two components, and examine the role of the reservoir chemical potential on just the third component. From **Figure 4a** through **Figure 4d**, we illustrate how to interpret an $x_{\text{Li}}-x_{\text{Mn}}-\mu_{\text{O}}$ diagram from the Li-Mn-O ternary convex hull. Each slice in **Figure 4a, b** is an isopleth between oxygen and a fixed $\text{Li}_x\text{Mn}_{1-x}$ ratio. The Li:Mn isopleth with a 1:2 ratio (purple), corresponding to LiMn_2O_4 , intersects both pure phases as well as 2-phase tie lines. By viewing the convex hull along this isoplethal slice in **Figure 4c**, we can use the intercept of tangent lines against the μ_{O} axis to illustrate the different phase transition and phase-coexistence regions. By repeating this process for all $\text{Li}_x\text{Mn}_{1-x}$ ratios, we can construct the full $x_{\text{Li}}-x_{\text{Mn}}-\mu_{\text{O}}$ diagram in **Figure 4d**. The right-side axis of **Figure 4c** shares the same color correspondence with the stability and coexistence regions in **Figure 4d**.

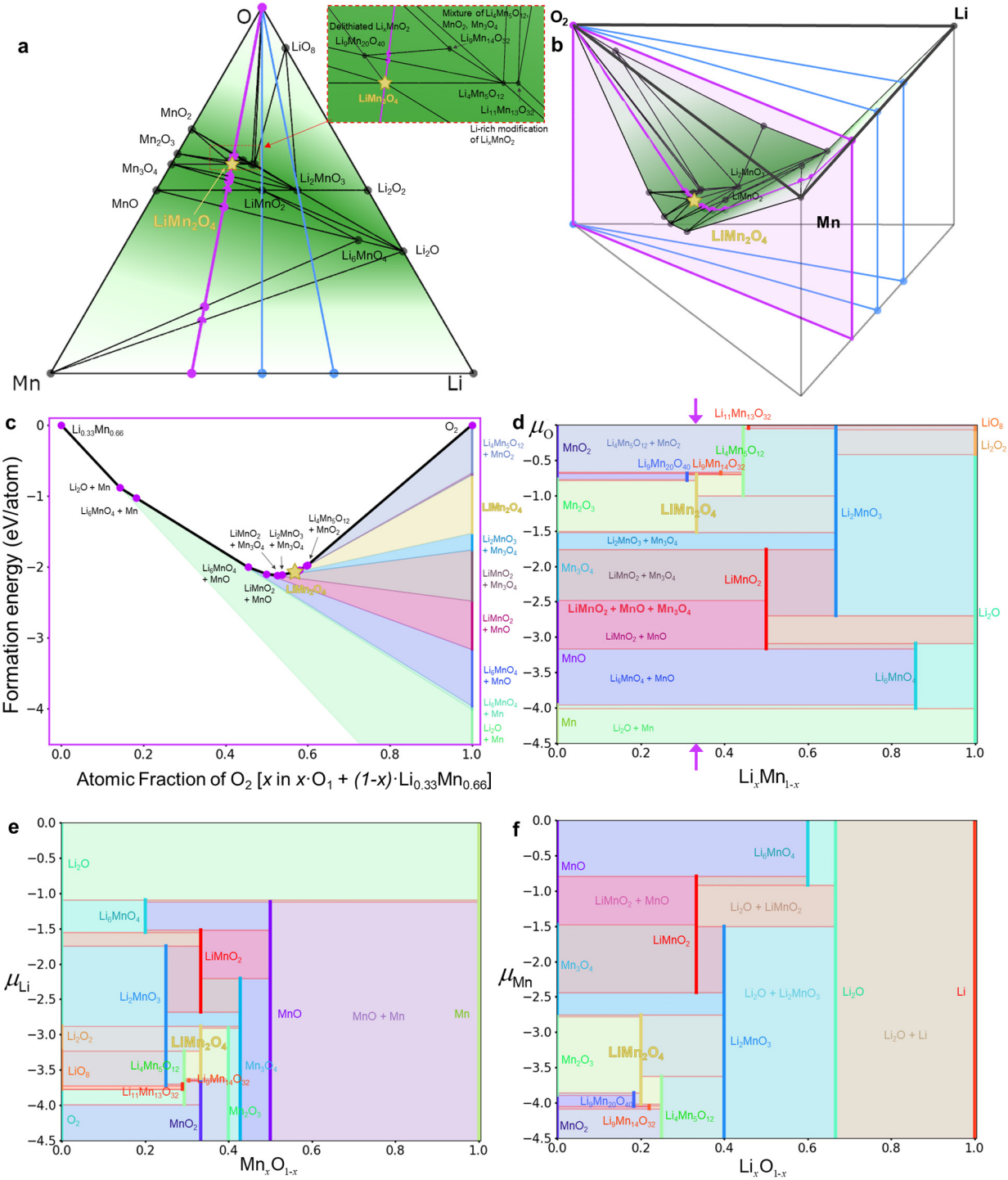


Figure 4. a) Ternary $x_{\text{Li}}\text{-}x_{\text{Mn}}\text{-}x_{\text{O}}$ convex hull. Inset shows DFT calculated-phases with ordered compositions, where $\text{Li}_9\text{Mn}_{20}\text{O}_{40}$ phase represents delithiated Li_xMnO_2 , the lithium-rich modification of LiMn_2O_4 is represented by $\text{Li}_{11}\text{Mn}_{13}\text{O}_{32}$, and the $\text{Li}_9\text{Mn}_{14}\text{O}_{32}$ phase represents a tie-line between $\text{MnO}_2\text{-Li}_4\text{Mn}_5\text{O}_{12}$. Isopleths between O_2 to $\text{Li}_{x}\text{Mn}_{1-x}$ are shown, with a purple highlight for a ratio of $\text{Li}:\text{Mn} = 1:2$. **b)** Ternary convex hull with energy axis, with isoplethal slices shown. **c)** Intercept rule construction of stability regions and phase coexistence along the μ_{O} axis. **d)** mixed $x_{\text{Li}}\text{-}x_{\text{Mn}}\text{-}\mu_{\text{O}}$ phase diagram, **e)** mixed $x_{\text{Mn}}\text{-}x_{\text{O}}\text{-}\mu_{\text{Li}}$ phase diagram, **f)** mixed $x_{\text{Li}}\text{-}x_{\text{O}}\text{-}\mu_{\text{Mn}}$ phase diagram. For the phase coexistence in $x_1\text{-}x_2\text{-}\mu_3$ diagram, single phases are vertical lines, 2-phase coexistence regions are rectangles that connects two single phases, and 3-phase coexistence regions are horizontal red lines that connects the ends of three single phases.

From the $x_{\text{Li}}-x_{\text{Mn}}-\mu_{\text{O}}$ in **Figure 4d**, we can examine reactions involving LiMn_2O_4 with O_2 gas, for example during synthesis or thermal decomposition. The μ_{O} for O_2 gas can be referenced to different temperatures and partial pressures using the earlier diagram from **Figure 3c**. The μ_{O} stability window for LiMn_2O_4 is between $[-1.5, -0.6]$ eV/atom; corresponding to temperature range around $600 - 900\text{K}$, for P_{O_2} ranges from $[0.21, 1]$ atm, corresponding to ambient atmosphere. This stability condition is in line with the reported solid-state synthesis temperatures of LiMn_2O_4 , which range from $700 - 1000\text{K}$ ^{46,47}, as well as the thermal decomposition temperature of LiMn_2O_4 at 1100K .⁴⁸ Additionally, compared to layered structure electrodes, such as LiMnO_2 , higher μ_{O} is beneficial for the stability of LiMn_2O_4 , which matches the experimental fact that the $\text{Mn}^{3+}/\text{Mn}^{4+}$ redox in LiMn_2O_4 requires a larger amount of oxygen redox to achieve high capacity, compared to $\text{Mn}^{2+}/\text{Mn}^{4+}$ in LiMnO_2 ⁴⁹.

To analyze lithiation process of LiMn_2O_4 for a given Mn:O ratio, we can utilize the $x_{\text{O}}-x_{\text{Mn}}-\mu_{\text{Li}}$ axis. As shown in **Figure 4e**, when we raise the voltage (thereby decreasing μ_{Li}) to charge LiMn_2O_4 , it undergoes oxidation and transforms into MnO_2 . We note that on the equilibrium phase diagram, the MnO_2 phase corresponds to the ground-state β (pyrolusite) phase, whereas for the real LiMn_2O_4 system, topotactic delithiation results in metastable λ - MnO_2 , which maintains the spinel framework. On the other hand, reducing the electrostatic potential (increasing μ_{Li}) can result in phase separation to $\text{Li}_2\text{MnO}_3 + \text{Mn}_3\text{O}_4$. The μ_{Li} window between -3.7 and -2.8 eV/atom corresponds to the phase transitions between MnO_2 and LiMn_2O_4 , as well as the transition from LiMn_2O_4 to LiMnO_2 .

For electrolyte stability, Mn dissolution from LiMn_2O_4 will occur if the μ_{Mn} is lower in the electrolyte than the lower-limit μ_{Mn} stability window in LiMn_2O_4 . For example, dissolution of Mn occurs if the applied μ_{Mn} in the electrolyte is below -4.1 eV, which as shown in **Figure 4f**, can induce multiple phase transformations to $\text{Li}_4\text{Mn}_5\text{O}_{12}$, $\text{Li}_9\text{Mn}_{20}\text{O}_{40}$, $\text{Li}_9\text{Mn}_{14}\text{O}_{32}$. To design an organic electrolyte that is resistant to Mn-dissolution, one needs to identify an organic electrolyte where the Mn-ion solvation energy overlaps the stability window of LiMn_2O_4 in the μ_{Mn} axis. To perform this analysis, one can construct the corresponding chemical potential diagram of the electrolyte from a convex hull using the same tangent line principles discussed here.

Oxidation of compositionally-complex alloys

Compositionally-complex alloys (CCAs) have near equimolar concentrations of multiple metal species, and in special cases form single-phase solid-solution high-entropy alloys (HEAs) and medium-entropy alloys (MEAs), which may have valuable properties for high-temperature materials for spacecraft and satellites,⁵⁰ corrosion-resistance for seawater treatment equipment,^{51,52} superior electron transport for electronic device, *etc.*^{53,54,55} However, discontinuous oxide granules or oxide layers can form when these alloys are exposed to O₂ atmospheres and high temperature. Although experimental measurements of the surface oxide phases formed in HEAs and MEAs are becoming more numerous,^{56,57} thermodynamic modeling remains sparse.⁵⁸ This may be due to the complexity of the possible binary, ternary, and quaternary oxides that compete to form during HEA/MEA oxidation.

To analyze the oxidation behaviors of multi-component alloys, we take CrCoNiO_x as a representative example. The chemical potential of oxygen in an HEAs depends on many factors, such as penetration depth of oxygen as it diffuses in, as well as the μ_O applied by the temperature and partial pressure of O₂ gas at the surface. The appropriate boundary conditions for this system are closed in the metal species, but with open exchange of volatile oxygen species. The relevant phase diagram is therefore closed with metal composition axes x_{Cr} - x_{Co} - x_{Ni} , and open with a μ_O axis. For the sake of visualization, we examine a here 3-metal MEA, however, the underlying geometric arguments and analyses are readily extendable to higher-component alloys.

Typically, phase diagrams for 4-component systems are viewed in barycentric coordinates using a 3D Gibbs tetrahedron to represent the quaternary convex hull, with 4 composition variables but no energy axis (**Figure 5a**). The energy axis can be recovered by constructing pseudo-ternary convex hulls by taking compounds as terminal points of the convex hull, and plotting the formation energy of phases relative to the terminal compounds, as illustrated in **Figure 5b**.

Each phase in the quaternary convex hull is a vertex, which we assign a color corresponding to the metal composition. We assign red, green, and blue to Co, Cr, and Ni, respectively. The color of binary through quaternary phases are then determined by their barycentric Co:Cr:Ni molar ratio. We use color saturation to correspond to the lowest critical oxygen chemical potential in which the phase is thermodynamically preferred to form, where white indicates pure O₂ gas.

Figure 5c, 5d shows two x_{Cr} - x_{Co} - x_{Ni} - μ_O phase diagrams at high and low μ_O ranges—split up to more clearly visualize the phase coexistence regions. By comparing the critical oxygen chemical potentials, we can extract the tendency of various metal constituents to oxidize; for example, Cr will oxidize at $\mu_O = -4$ eV to form a protective Cr₂O₃ scale, which is before Ni and Co which both oxidize around $\mu_O = -2.5$ eV. Experimentally, the oxidation of equimolar CrCoNi is shown to form only a Cr₂O₃ layer^{53,54,56}, as anticipated by these diagrams. Additionally, a mixed spinel (Co,Ni)Cr₂O₄ is experimentally observed^{53,54,56,59}, which in our phase diagram on **Figure 5c** may correspond to a solid-solution that would form along the tie line between CoNi₂O₄ and CrNiO₄.

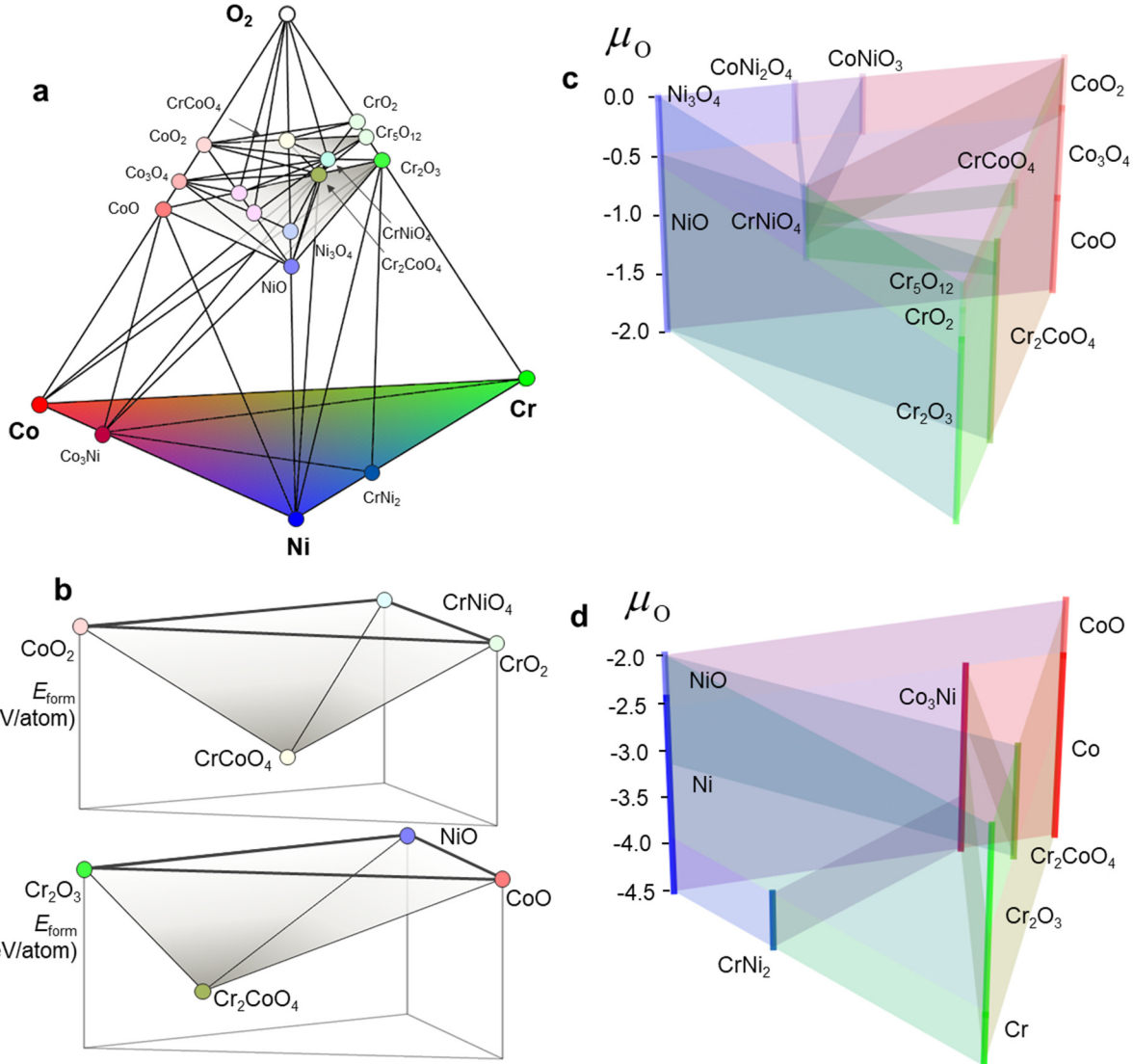


Figure 5. **a)** Quaternary $X_{\text{Co}}-X_{\text{Cr}}-X_{\text{Ni}}-X_{\text{O}}$ convex hull. Each single phase is assigned a color based on metal composition of Cr:Co:Ni ratio, and a transparency based on the lowest critical μ_{O} for a given phase. Two triangular ternary isopleths are shown in gray colorscale, connecting $\text{CoO}_2-\text{CrNiO}_4-\text{CrO}_2$, and $\text{Cr}_2\text{O}_3-\text{NiO}-\text{CoO}$. **b)** Pseudo-ternary convex hulls with a recovered formation energy axis, with energies referenced to the terminal compound phases. **c)** Mixed $x_{\text{Cr}}-x_{\text{Co}}-x_{\text{Ni}}-\mu_{\text{O}}$ phase diagram, where **c)** μ_{O} in $[-2.0, 0.0]$ eV/atom, and **d)** μ_{O} in $[-4.5, -2.0]$ eV/atom.

In **Figure 5c, 5d**, each single phase is a vertical line, a 2-phase coexistence region is vertical rectangle plane bounded by two single phase lines, a 3-phase coexistence region is a triangular prism formed by three single phase lines, and finally a 4-phase coexistence region is a horizontal triangle connected by two 3-phase coexistence triangular prisms. Although 2-phase coexistence regions and 4-phase coexistence regions are both 2-D manifolds, they have different physical interpretations because there is no degree of freedom for changing μ_{O} in 4-phase coexistence, leading to a horizontal 2D region, whereas we can change μ_{O} in 2-phase coexistence, leading to a vertical 2D region.

Dimensionality of Coexistence Regions in Mixed Diagrams

As discussed in Part I of this 3-part series, the essential geometric object corresponding to phase coexistence is the simplicial polytope, which is an N -dimensional analogue of a triangle. The counting relations between the vertices, edges, and facets of a simplicial polytope are given by the Dehn-Sommerville relations, which takes a similar form to Pascal's triangle. For example, a 4-phase coexistence tetrahedron is a 3-dimensional simplex, which has ${}_4C_1 = 4$ vertices (single phases), ${}_4C_2 = 6$ edges (2-phase coexistence), ${}_4C_3 = 4$ triangles (3-phase) and ${}_4C_4 = 1$ tetrahedron (4-phase). Even when one performs a Legendre transformation, the fundamental underlying geometric structure of the $U(S, X)$ simplex, as well as its coexistence regions, are preserved.

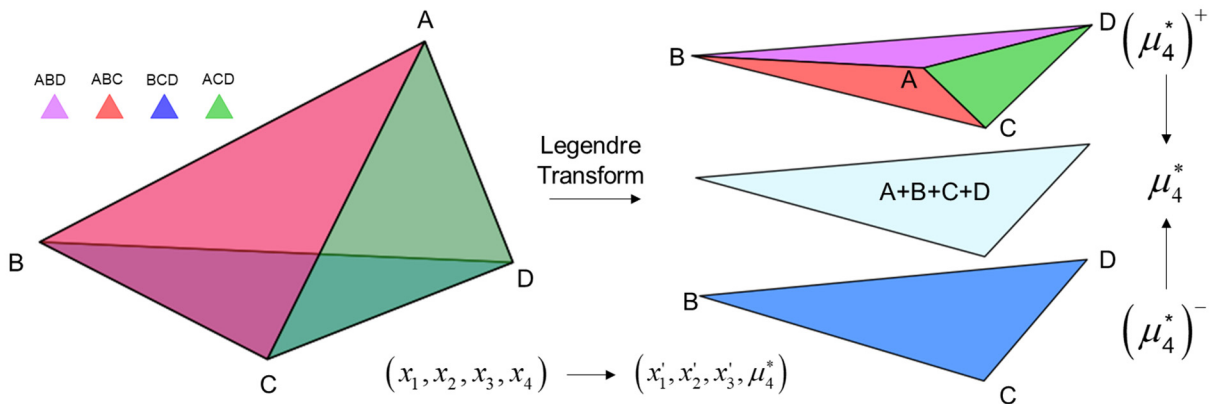


Figure 6. A 3D simplicial polytope (a tetrahedron) with extensive natural variables is smushed via a Legendre transformation to a fixed intensive variable of μ_4^* . All simplicial facets from the tetrahedron, and thereby its phase coexistence information, remains preserved following the Legendre transformation.

On a four-phase coexistence tetrahedron, all vertices share the same chemical potentials μ_1 through μ_4 . On composition axes, the coordinates for each vertex can be written as (x_1, x_2, x_3, x_4) , where 1, 2, 3, 4 correspond to different elements, and $x_4 = 1 - x_1 - x_2 - x_3$ by the affine constraint. Upon a Legendre transformation from x_4 to μ_4 , the x_4 coordinates all change to the same μ_4 , which effectively smushes all the vertices, edges and facets from the tetrahedron onto a single μ_4^* value, as illustrated in **Figure 6**. Each x_i coordinate then changes to x_i' by the new affine constraint, $x_3' = 1 - x_1' - x_2'$.

Importantly, all the 2-phase edges, 3-phase triangles, and the 4-phase tetrahedron are preserved after the Legendre transformation. The Legendre transformation does not generate any new phase coexistence information, nor does it lose any information. It simply provides a different perspective, but for the same equilibrium of heterogeneous substances. On mixed phase diagrams the phase coexistence regions no longer appear like simplicial polytopes, but are in fact down-projections of the high-dimensional simplices from the $U(S, X_i)$ space where they originated. In the **SI5**, we provide tables that explicitly describe the dimensionality of coexistence regions on mixed phase diagrams. These the geometric considerations of phase coexistence are the same with any other intensive variable as well, for example on a traditional ternary composition phase diagram (x_1, x_2, x_3, T) , or replacing μ_4 with pressure, magnetic field, area-to-volume ratio, *etc.*

Duality in Thermodynamics

Duality gives *two different points of view of looking at the same object*. As summarized in the table below, there is a duality in thermodynamics between open and closed systems; which corresponds to a duality between the Internal Energy potential and its Legendre transformation; which corresponds to a duality in computation between a convex hull and its half-space intersection. Our implementation of these duality concepts for chemical work are geometrically identical to the duality relationships between the Maxwell $U(S,V)$ surface and the $G(T,P)$ free energy surfaces which we are commonly familiar with today. Our primary contribution here was to extend these concepts from the $G(T,P,x)$ space to the grand potential $\phi(T,P,\mu)$ space. The dualities in macroscopic boundary conditions for classical thermodynamics can further be linked to dualities at the atomistic scale, in the statistical mechanics description between an NVT canonical ensemble and the μVT grand canonical ensemble.

Duality in Thermodynamics		
Thermodynamic System	Closed equilibrium mixture of heterogeneous substances	Subsystem of single material open to an external reservoir
Thermodynamic Potential	Internal Energy $U(X_i)$ with extensive natural variables	Legendre transformation to $\Phi(Y_i)$ with natural intensive variable
Computational Thermodynamics	Convex hull of vertices	Half-space intersection of hyperplanes

Our motivation for this work was to address the underutilization of chemical potential diagrams in the existing materials thermodynamics literature. Although computational tools for chemical potential diagrams have existed for over two decades, we believe that the bottleneck to their widespread proliferation is not their computation, but rather, is the physical understanding and interpretation of these diagrams. In particular, chemical potential diagrams offer a unique connection to the kinetics of diffusion, nucleation and growth, which has broad and obvious value in materials science and engineering. Therefore, the essential intellectual task in deploying chemical potential diagrams (or any phase diagram for that matter) is connecting a physical scenario to its boundary conditions and corresponding thermodynamic potential, and then from the available thermochemical data to the computation of a final phase diagram.

In framing open boundary conditions to analyze the stability of a material-of-interest with respect to an open reservoir, the next question becomes, how can one control the relative stability of a target material, when there may be numerous forms of available work? In Part III of this series, we derive a generalized Clausius-Clapeyron relation to examine the gradients of phase boundaries on high-dimensional phase diagrams, providing a pathway to control the relative stability of specific phases.

Code Availability

All code for analyzing and visualizing convex hull, high dimensional chemical potential diagrams, and mixed composition-chemical potential diagrams can be found on Github at the following link:

https://github.com/dd-debug/chemical_potential_diagram_and_convex_hull_and_pourbaix_diagram

The link includes a readme, tutorial example files, installation guide, Python package requirements, and instructions for use.

Acknowledgements

This work was supported as part of GENESIS: A Next Generation Synthesis Center, an Energy Frontier Research Center funded by the US Department of Energy, Office of Science, Basic Energy Sciences (award No. DE-SC0019212).

References

¹ Atiyah, M. F. "Duality in mathematics and physics." *Conferències FME* 5 (2007): 2007-2008.

² Gibbs, Josiah Willard, and Edwin Bidwell Wilson. *Vector analysis: A text-book for the use of students of mathematics and physics, founded upon the lectures of j. willard gibbs.* Yale University Press, 1901.

³ Fathi, Mohammad Bagher. "History of the reciprocal lattice." *Powder Diffraction* 34.3 (2019): 260-266.

⁴ Yokokawa, H. "Generalized chemical potential diagram and its applications to chemical reactions at interfaces between dissimilar materials." *Journal of phase equilibria* 20.3 (1999): 258-287.

⁵ Ahmad, E. A., et al. "Thermodynamic stability of LaMnO₃ and its competing oxides: A hybrid density functional study of an alkaline fuel cell catalyst." *Physical Review B* 84.8 (2011): 085137.

⁶ <https://onlinelibrary.wiley.com/doi/abs/10.1002/adma.200700843>

⁷ Reuter, Karsten, and Matthias Scheffler. "First-principles atomistic thermodynamics for oxidation catalysis: surface phase diagrams and catalytically interesting regions." *Physical review letters* 90.4 (2003): 046103.

⁸ Reuter, Karsten, and Matthias Scheffler. "Composition, structure, and stability of RuO₂ (110) as a function of oxygen pressure." *Physical Review B* 65.3 (2001): 035406.

⁹ Kitchin, John R., Karsten Reuter, and Matthias Scheffler. "Alloy surface segregation in reactive environments: first-principles atomistic thermodynamics study of Ag₃Pd (111) in oxygen atmospheres." *Physical Review B* 77.7 (2008): 075437.

¹⁰ Korte-Kerzel, Sandra, et al. "Defect phases-thermodynamics and impact on material properties." *International Materials Reviews* 67.1 (2022)

¹¹ Freysoldt, Christoph, et al. "First-principles calculations for point defects in solids." *Reviews of modern physics* 86.1 (2014): 253.

¹² Todd, Paul K., et al. "Selectivity in yttrium manganese oxide synthesis via local chemical potentials in hyperdimensional phase space." *Journal of the American Chemical Society* 143.37 (2021): 15185-15194.

¹³ Chen, Jiadong, et al. "Navigating phase diagram complexity to guide robotic inorganic materials synthesis." *arXiv preprint arXiv:2304.00743* (2023).

¹⁴ Wen, Mingjian, et al. "Chemical reaction networks and opportunities for machine learning." *Nature Computational Science* 3.1 (2023): 12-24.

¹⁵ Feinberg, Martin. "Foundations of chemical reaction network theory." (2019).

¹⁶ Jackson, Adam J., Davide Tiana, and Aron Walsh. "A universal chemical potential for sulfur vapours." *Chemical science* 7.2 (2016): 1082-1092.

¹⁷ Nair, Sreejith, et al. "Solid-source metal-organic MBE for elemental Ir and Ru films." *Journal of Vacuum Science & Technology A* 41.6 (2023).

¹⁸ Sun, Wenhao, et al. "Non-equilibrium crystallization pathways of manganese oxides in aqueous solution." *Nature communications* 10.1 (2019): 573.

¹⁹ Richards, William D., et al. "Interface stability in solid-state batteries." *Chemistry of Materials* 28.1 (2016): 266-273.

²⁰ Zhu, Yizhou, Xingfeng He, and Yifei Mo. "Origin of outstanding stability in the lithium solid electrolyte materials: insights from thermodynamic analyses based on first-principles calculations." *ACS applied materials & interfaces* 7.42 (2015): 23685-23693.

²¹ Callen, Herbert B., and H. L. Scott. "Thermodynamics and an Introduction to Thermostatistics." (1998): 164-167.

²² Zia, Royce KP, Edward F. Redish, and Susan R. McKay. "Making sense of the Legendre transform." *American Journal of Physics* 77.7 (2009): 614-622.

²³ Jain, Anubhav, et al. "Commentary: The Materials Project: A materials genome approach to accelerating materials innovation." *APL materials* 1.1 (2013).

²⁴ Ong, Shyue Ping, et al. "Li–Fe–P–O₂ phase diagram from first principles calculations." *Chemistry of Materials* 20.5 (2008): 1798-1807.

²⁵ Hautier, Geoffroy, et al. "Accuracy of density functional theory in predicting formation energies of ternary oxides from binary oxides and its implication on phase stability." *Physical Review B* 85.15 (2012): 155208.

²⁶ Kirklin, Scott, et al. "The Open Quantum Materials Database (OQMD): assessing the accuracy of DFT formation energies." *npj Computational Materials* 1.1 (2015): 1-15.

²⁷ Wang, Amanda, et al. "A framework for quantifying uncertainty in DFT energy corrections." *Scientific reports* 11.1 (2021): 15496.

²⁸ Jain, Anubhav, et al. "Formation enthalpies by mixing GGA and GGA+ U calculations." *Physical Review B* 84.4 (2011): 045115.

²⁹ Kingsbury, Ryan S., et al. "A flexible and scalable scheme for mixing computed formation energies from different levels of theory." *npj Computational Materials* 8.1 (2022): 195.

³⁰ Jang, Jun Tae, et al. "Study on the photoresponse of amorphous In–Ga–Zn–O and zinc oxynitride semiconductor devices by the extraction of sub-gap-state distribution and device simulation." *ACS applied materials & interfaces* 7.28 (2015): 15570-15577.

³¹ Ahmed, Manan, and Guo Xinxin. "A review of metal oxynitrides for photocatalysis." *Inorganic Chemistry Frontiers* 3.5 (2016): 578-590.

³² Young, Samuel D., et al. "Metal oxynitrides for the electrocatalytic reduction of nitrogen to ammonia." *The Journal of Physical Chemistry C* 126.31 (2022): 12980-12993.

³³ Zhang, Zongbo, et al. "Hydrophobic, transparent and hard silicon oxynitride coating from perhydropolysilazane." *Polymer International* 64.8 (2015): 971-978.

³⁴ Yu, Minghao, et al. "Holey tungsten oxynitride nanowires: novel anodes efficiently integrate microbial chemical energy conversion and electrochemical energy storage." *Advanced materials* 27.19 (2015): 3085-3091.

³⁵ Young, Samuel D., et al. "Thermodynamic Stability and Anion Ordering of Perovskite Oxynitrides." *Chemistry of Materials* 35.15 (2023): 5975-5987.

³⁶ Harada, Jaye K., et al. "Heteroanionic materials by design: Progress toward targeted properties." *Advanced Materials* 31.19 (2019): 1805295.

³⁷ Kageyama, Hiroshi, et al. "Expanding frontiers in materials chemistry and physics with multiple anions." *Nature communications* 9.1 (2018): 772.

³⁸ Caskey, Christopher M., et al. "Thin film synthesis and properties of copper nitride, a metastable semiconductor." *Materials Horizons* 1.4 (2014): 424-430.

³⁹ Sun, Wenhao, et al. "The thermodynamic scale of inorganic crystalline metastability." *Science advances* 2.11 (2016): e1600225.

⁴⁰ Thackeray, Michael M. "Manganese oxides for lithium batteries." *Progress in Solid State Chemistry* 25.1-2 (1997): 1-71.

⁴¹ Deng, Yuanfu, et al. "Recent advances in Mn-based oxides as anode materials for lithium ion batteries." *Rsc Advances* 4.45 (2014): 23914-23935.

⁴² Lee, Jinhyuk, et al. "Unlocking the potential of cation-disordered oxides for rechargeable lithium batteries." *science* 343.6170 (2014): 519-522.

⁴³ Thackeray, M. M., et al. "Electrochemical extraction of lithium from LiMn₂O₄." *Materials Research Bulletin* 19.2 (1984): 179-187.

⁴⁴ Lee, Byungju, et al. "First-principles study of the reaction mechanism in sodium–oxygen batteries." *chemistry of Materials* 26.2 (2014): 1048-1055.

⁴⁵ Huang, Yimeng, et al. "Lithium manganese spinel cathodes for lithium-ion batteries." *Advanced Energy Materials* 11.2 (2021): 2000997.

⁴⁶ Macklin, W. J., R. J. Neat, and R. J. Powell. "Performance of lithium manganese oxide spinel electrodes in a lithium polymer electrolyte cell." *Journal of power sources* 34.1 (1991): 39-49.

⁴⁷ Momchilov, A., et al. "Rechargeable lithium battery with spinel-related MnO₂ II. Optimization of the LiMn₂O₄ synthesis conditions." *Journal of power sources* 41.3 (1993): 305-314.

⁴⁸ Buzanov, G. A., et al. "Phase equilibria involving solid solutions in the Li–Mn–O system." *Russian Journal of Inorganic Chemistry* 62 (2017): 551-557.

⁴⁹ Lee, Jinhyuk, et al. "Reversible Mn²⁺/Mn⁴⁺ double redox in lithium-excess cathode materials." *Nature* 556.7700 (2018): 185-190.

⁵⁰ Sharma, Aayush, et al. "Atomistic clustering-ordering and high-strain deformation of an Al0.1CrCoFeNi high-entropy alloy." *Scientific reports* 6.1 (2016): 31028.

⁵¹ Qiu, Yao, et al. "Corrosion of high entropy alloys." *npj Materials degradation* 1.1 (2017): 15.

⁵² Chen, Ganlin, et al. "Stability and growth kinetics of {112} twin embryos in β -Ti alloys." *Acta Materialia* 263 (2024): 119520.

⁵³ Agustianingrum, Maya Putri, Unhae Lee, and Nokeun Park. "High-temperature oxidation behaviour of CoCrNi medium-entropy alloy." *Corrosion Science* 173 (2020): 108755.

⁵⁴ Stephan-Scherb, Christiane, et al. "High-temperature oxidation in dry and humid atmospheres of the equiatomic CrMnFeCoNi and CrCoNi high-and medium-entropy alloys." *Oxidation of Metals* 95 (2021): 105-133.

⁵⁵ Evans, Daniel, et al. "Visualizing temperature-dependent phase stability in high entropy alloys." *npj Computational Materials* 7.1 (2021): 151.

⁵⁶ Kai, W., et al. "High-temperature air-oxidation of NiCoCrAl_x medium-entropy alloys." *Corrosion Science* 192 (2021): 109858.

⁵⁷ Jiang, Dong, et al. "High-temperature oxidation behaviors of an equiatomic CrMnFeCoNi high entropy alloy." *Materials Today Communications* 32 (2022): 104185.

⁵⁸ Butler, Todd M., and Mark L. Weaver. "Oxidation behavior of arc melted AlCoCrFeNi multi-component high-entropy alloys." *Journal of Alloys and Compounds* 674 (2016): 229-244.

⁵⁹ Schaefer, Seth C. *Electrochemical determination of thermodynamic properties of NiCr₂O₄ and CoCr₂O₄*. No. 9043. US Department of the Interior, Bureau of Mines, 1986.

The geometry of high-dimensional phase diagrams:

II. The duality between closed and open chemical systems

Jiadong Chen¹, Matthew J. Powell-Palm², Wenhao Sun^{1*}

¹Department of Materials Science and Engineering, University of Michigan, Ann Arbor, MI, 48109, USA

²J. Mike Walker '66 Department of Mechanical Engineering, Texas A&M University, College Station, TX, 77802, USA

³Department of Materials Science & Engineering, Texas A&M University, College Station, TX, 77802, USA

*Correspondence to: whsun@umich.edu

Supplemental Information

Contents

SI1. The Legendre Transformation and Point-Line Duality	2
SI2. Duality between convex hulls and half-space intersections.....	4
SI3. Computation of chemical potential diagrams.....	7
SI3.1. Linearization assumption	7
SI3.2 Computation of chemical potential diagrams through the Intercept Rule.....	7
SI3.3. Computation of chemical potential diagrams through half-space intersection	8
SI3.3.1. Phase diagram with all chemical potential axes	8
SI3.3.2. Equilibrium Envelope	9
SI4. Computation of mixed composition/chemical potential diagrams	10
SI4.1. $\mu_1-\mu_2-x_3$ phase diagram ($x_{\text{Ta}}-\mu_0-\mu_N$)	10
SI4.1. $\mu_1-x_2x_3$ phase diagram ($\mu_{\text{Li}}-x_{\text{Mn}}x_0$).....	11
SI4.3. $\mu_1-x_2-x_3-x_4$ phase diagram ($\mu_0-x_{\text{Ni}}-x_{\text{Cr}}-x_{\text{Co}}$).....	11
SI5. A generalized phase rule for mixed μ-x diagrams.....	13

SI1. The Legendre Transformation and Point-Line Duality

There is a duality between a convex curve and its envelope of tangent planes. In projective geometry, this duality is called *Point-Line Duality*, where the convex curve is referred to as the ‘primal’ surface, and the envelope of tangent planes is the ‘dual’ surface. This dual surface encodes the inclination of the tangent planes for the Internal Energy surface—in other words, it redefines the conjugate intensive variable as the natural variable. This process is performed by the Legendre transformation, which defines a new thermodynamic potential Φ , by a change in natural variable from an extensive variable X to intensive variable Y . The general expression can be written as: $\Phi = U - XY$, where $Y = \partial U / \partial X$. For example, the Helmholtz potential, $F(T, V) = U - TS$, replaces the extensive variable S with its intensive conjugate T , and the Gibbs potential, $G(T, P) = U + PV - TS$, further replaces volume with pressure.

In **Figure S1**, we illustrate a transformation of the Internal Energy $U(S)$ to the Helmholtz free energy $F(T)$. If a thermodynamic system is in contact with an external temperature reservoir, then when the system reaches equilibrium with the external reservoir, U should be minimized *under a constraint* where the externally applied temperature is some T_1 . This is shown as a tangent line with slope as $\partial U / \partial S = T_1$, as illustrated by the red line in **Figure S1a**. A new thermodynamic condition is then defined through Legendre transformation, $F(T_1) = U_1 - (\partial U / \partial S)_{T_1} S_1$.

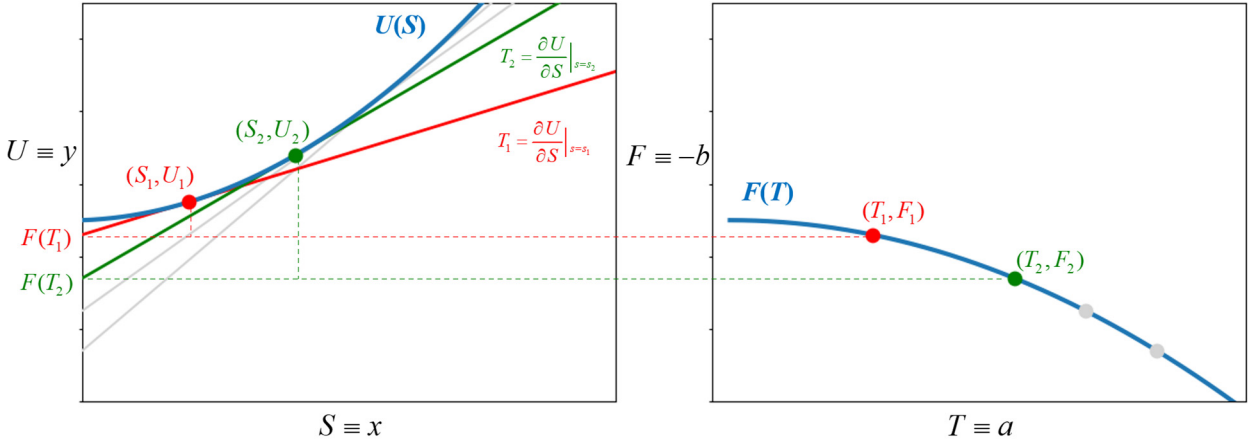


Figure S1. Schematic relationship between (a) U and S , (b) F and T , at fixed volume for homogenous phases. $[S, U]$ and $[T, F]$ are dual spaces and the two blue curves are duality of each other.

On **Figure S1**, $F(T_1)$ corresponds to the point at $S = 0$. In other words, $F(T_1)$ is the y -intercept of the tangent line to $U(S)$ at the point where $\partial U/\partial S = T_1$. More generally speaking, $F(T) = U - (\partial U/\partial S)S = U - TS$, which encodes the information of $U(S)$, but without a dependence on S . The natural variable of F is now T , and the differential form is $dF = -SdT$.

If we traverse all points on the $U(S)$ curve with different values of $T = \partial U/\partial S$, we can trace out the $F(T)$ curve which is shown in **Figure S1b**. Based on the stability criterion for homogenous phases, U is *convex up* with respect to extensive variables, so $\partial^2 U/\partial S^2 > 0$. Because $\partial^2 U/\partial S^2 = T/c_v$, where c_v is the heat capacity at constant volume, this stability criterion implies that heat capacity for a self-stable phase must be positive. If we trace F with respect to T , we notice the curve is *concave*, $\partial^2 F/\partial T^2 < 0$. This negative curvature in $F(T)$ is also a consequence of the positive heat capacity of materials.

Point-Line Duality and the Legendre Transformation

As discussed in the manuscript, *Point-Line Duality* leverages the duality between a line $y = ax - b$ in primal $[x, y]$ space, to a point (a, b) in dual $[a, b]$ space. In thermodynamics, from **Figure S1**, we can reformulate the tangent line to $U(S)$ as: $y = ax - b \rightarrow U = TS + F$. Here, the correspondence is $U \equiv y$, $T \equiv a$, $S \equiv x$, and $F \equiv -b$; meaning that $[U, S]$ and $[-F, T]$ are dual spaces. Since $-F$ and F show one-to-one correspondence, we can also say that $[U, S]$ and $[F, T]$ spaces are dual with each other. In **Figure S1**, for each line on the $U(S)$ curve, we can draw its dual point in $[F, T]$ space, shown by the green and red lines in $[U, S]$ space and points in $[F, T]$ space. In this sense, the blue convex $U(S)$ curve is dual to its corresponding concave $F(T)$ curve.

In higher dimensions $d > 2$, the corresponding notion is *Point-Hyperplane duality*, where a hyperplane is defined as a $d-1$ dimensional subspace which splits a space into two half-spaces. The hyperplane can be defined in the primal $[x, y]$ space as $y = \sum_{i=1}^{d-1} a_i x_i - b$, while the corresponding point in the dual $[a, b]$ space is (a_1, \dots, a_{n-1}, b) . The above discussion is generalized in **Table S1**, which gives the corresponding relationships between points and lines in different dual spaces. In thermodynamics, we should treat the primal space in its multidimensional form of $U(S, X_1, \dots, X_i)$, with the energy scalar U as the y -axis, and the various extensive variables as corresponding to the x_i terms.

Table S1. Table of the Point-Line duality between primal $[x, y]$ space and dual $[a, b]$ space.

		Primal	Dual
		Point	Hyperplane
2 dimensional		$[x, y]$	$[a, b]$
N -dimensional		$[x_1, x_2, \dots, x_{n-1}, y]$	$[a_1, \dots, a_{n-1}, b]$
2 dimensional		(x, y)	$b = xa - y$
N -dimensional		$(x_1, x_2, \dots, x_{n-1}, y)$	$b = \sum_{i=1}^{d-1} x_i a_i - y$

SI2. Duality between convex hulls and half-space intersections

From a materials thermodynamics standpoint, Point-Line Duality holds particular significance as it is related to the duality between G - x convex hulls and their corresponding half-space intersections, which are Φ - μ chemical potential diagrams. As a definition of half-space intersection: a line in a plane separates the plane into two sections, each of which is called a half-plane; in higher dimensions, the notion is half-space. Half-space intersections forms an inner envelope. Here, we provide a mathematical derivation of this duality relationship, and show its relevance to thermodynamic phase diagrams, which proves the duality between the composition vs. chemical potential phase diagrams.

Consider a set of points, P , in primal space. As shown in **Figure S2**, a point $p \in P$ is a vertex of a lower convex hull, $\mathcal{LH}(P)$, if and only if there is a non-vertical line l passing through p such that all other points of P lie above l . Correspondingly, in dual space, represented by an asterisk, the line segment $p^* \in P^*$ is a part of the lower envelope ($\mathcal{LE}(P^*)$ half-space hyperplanes), if and only if there is a point l^* on the line p^* such that l^* lies below all other lines of P^* .

These arguments generalize to N -dimensional spaces, where for a N -dimensional point $p \in P$ to be a vertex of an N -dimensional lower convex hull, there must be a non-vertical hyperplane l , passing through p such that all other points of P lie above l . The dual statement is that for a hyperplane $p^* \in P^*$ to be a part of a lower envelope, there is a point l^* on the plane p^* , such that l^* lies below all other lines of P^* . In projective geometry, $[x, y]$ and $[a, b]$ are dual to one another, but in thermodynamics $[U, S]$ and $[-F, T]$ are dual to one another, meaning that the lower envelope from projective geometry becomes an upper envelope when applied to thermodynamics.

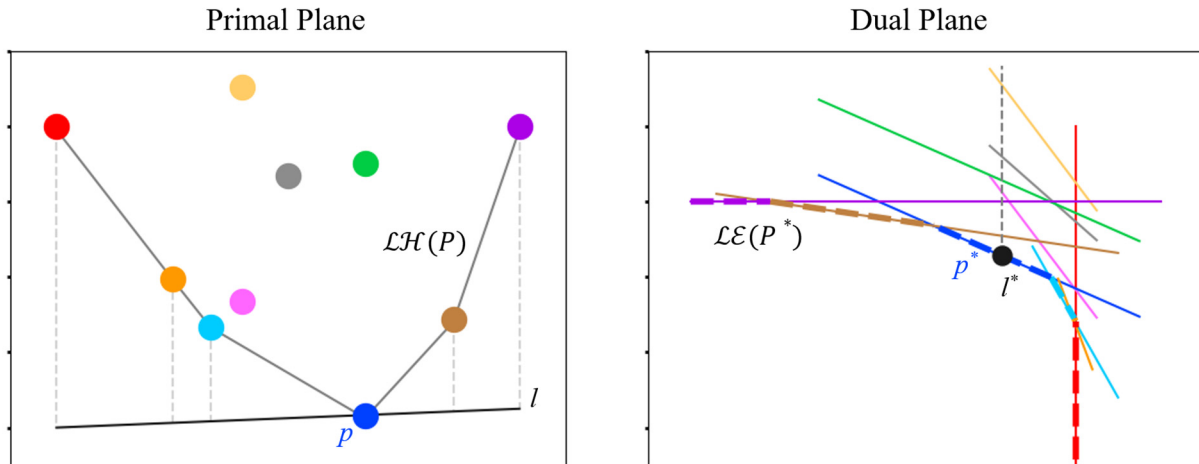


Figure S2. The duality between a lower convex hull and a lower envelope. Colors of points in the primal space correspond to their lines in the dual space.

Similarly, in this study, a set of points in the convex hull G - x primal space, are represented by a set of hyperplanes in the chemical potential diagram ϕ - μ space, forming the half-space intersections. In the same way that $F(T)$ is a Legendre transformation of $U(S)$, and therefore is its dual, we can perform a similar Legendre transformation from $G(x)$ to the grand potential, $\phi(\mu)$. At constant temperature and pressure, this can be defined as:

$$\bar{G}(T, P, x_1, x_2 \dots x_n) \xrightarrow{LT} \bar{\phi}(T, P, \mu_1, \mu_2 \dots \mu_n)$$

$$\phi = G - \sum_{i=1}^n \frac{\partial \bar{G}}{\partial x_i} x_i = G - \sum_{i=1}^n \mu_i x_i$$

For each phase, which is given by a vertex in G - x_1 - x_2 space, its corresponding Grand free energy is given by $\phi = G - \sum_{i=1}^n \mu_i x_i$. Taking a binary Mn-O system as an example, this Grand free energy is written as $\phi = G - \mu_{\text{Mn}} x_{\text{Mn}} - \mu_{\text{O}} x_{\text{O}}$. Although the binary convex hull can be fully represented with either x_{Mn} or x_{O} , as $x_{\text{Mn}} = 1 - x_{\text{O}}$, for a duality analysis we can include the redundant x_2 information. Therefore, a point in $[x_{\text{Mn}}, x_{\text{O}}, \bar{G}]$ space corresponds to a 2-D hyperplane in $[\mu_{\text{Mn}}, \mu_{\text{O}}, \bar{\phi}]$ space.

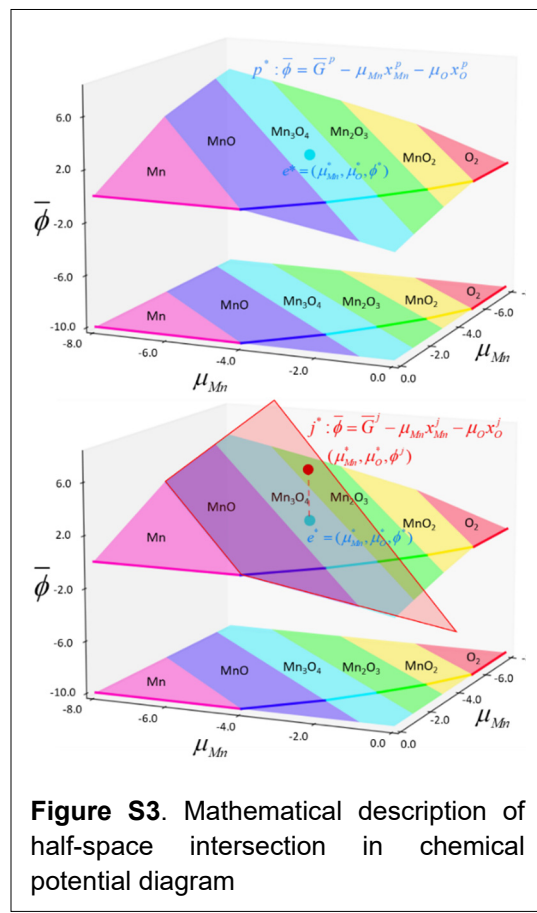


Figure S3. Mathematical description of half-space intersection in chemical potential diagram

Based on the way $\bar{\phi}$ is defined, a phase p on the Mn-O convex hull can be represented by the plane equation p^* as $\bar{\phi} = \bar{G}^p - \mu_{\text{Mn}} x_{\text{Mn}}^p - \mu_{\text{O}} x_{\text{O}}^p$, where x_{O}^p , x_{Mn}^p , \bar{G}^p represents composition of oxygen, manganese, and Gibbs formation free energy per atom of Mn_3O_4 . Then, because e^* is a point on the plane p^* , we have $\bar{\phi}^* = \bar{G}^p - \mu_{\text{Mn}}^* x_{\text{Mn}}^p - \mu_{\text{O}}^* x_{\text{O}}^p$

In **Figure S3**, for a plane $\text{Mn}_3\text{O}_4 p^* \in P^*$ to be a part of a lower envelope in $[\mu_{\text{Mn}}, \mu_{\text{O}}, \bar{\phi}]$ space, there is a point $e^* = (\mu_{\text{Mn}}^*, \mu_{\text{O}}^*, \bar{\phi}^*)$ on the plane p^* , such that e^* lies **below** all other planes of P^* . In other words, for any plane $j^* \in \{i \mid i \in P^*, i \neq p^*\}$, where j^* is $\bar{\phi} = \bar{G}^j - \mu_{\text{Mn}} x_{\text{Mn}}^j - \mu_{\text{O}} x_{\text{O}}^j$, $\bar{\phi}^*$ should be no greater than the corresponding $\bar{\phi}^j$ value at $\mu_{\text{Mn}}^*, \mu_{\text{O}}^*$ on the plane j^* . Mathematically, this means at $\mu_{\text{Mn}}^*, \mu_{\text{O}}^*$:

$$\bar{\phi}^* \leq \bar{\phi}^j \quad \text{Eq. S1}$$

Therefore, if **Eq. 1** is true, there exists a point e^* on the plane p^* such that the e^* is below any other plane j^* . This means p^* is on the lower half-space intersection envelope.

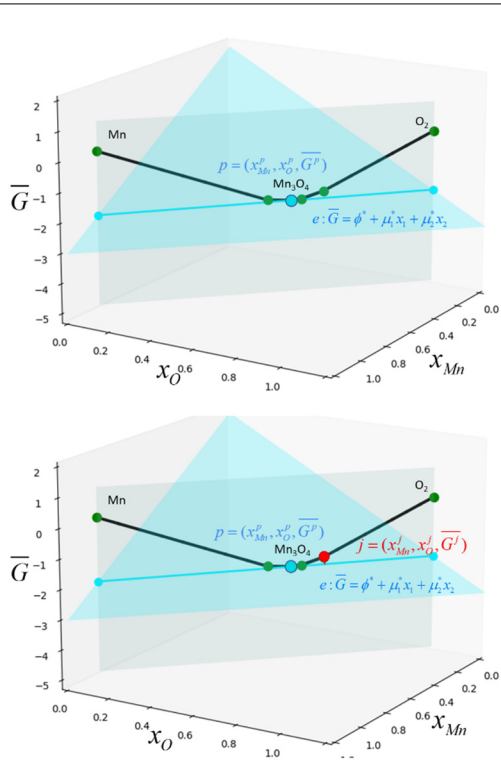


Figure S4. Mathematical description of convex hull in formation energy and composition phase diagram.

For a point $e^* = (\mu_{Mn}^*, \mu_O^*, \bar{\phi}^*)$ on plane p^* in $[\mu_{Mn}, \mu_O, \bar{\phi}]$ space, its dual plane e in $[x_{Mn}, x_O, \bar{G}]$ space is $\bar{G} = \bar{\phi}^* + \mu_{Mn}^* x_{Mn} + \mu_O^* x_O$, as shown as the light blue triangle in Figure S4. Every points on this plane has same chemical potentials. Then the dual of p^* is $p = (x_{Mn}^p, x_O^p, \bar{G}^p)$, which is material Mn_3O_4 . If p is a vertex on the convex hull, there is a plane e passing through p , and below all other vertices from P (all other materials).

This means for any point $j \in \{i \mid i \in P, i \neq p\}$, where $j = (x_{Mn}^j, x_O^j, \bar{G}^j)$, \bar{G}^j should be greater than the corresponding \bar{G}^e value on the plane e at x_{Mn}^j, x_O^j , as shown as the red point on the convex hull of left figure. Mathematically, this means at x_{Mn}^j, x_O^j :

$$\bar{G}^e \leq \bar{G}^j$$

Since $\bar{G}^e = \bar{\phi}^* + \mu_{Mn}^* x_{Mn}^j + \mu_O^* x_O^j$, we can substitute \bar{G}^e and rearrange the inequality as:

$$\bar{\phi}^* \leq \bar{G}^j - \mu_{Mn}^* x_{Mn}^j - \mu_O^* x_O^j$$

Here, the right-hand side is $\bar{\phi}^j$ at μ_{Mn}^*, μ_O^* . So, the inequality is equal at μ_{Mn}^*, μ_O^* to

$$\bar{\phi}^* \leq \bar{\phi}^j \quad \text{Eq. S2}$$

If Eq. S2 is true, then there is a plane e passing through p and below all other points, which means p is a vertex on the convex hull. Eq. 1 and Eq. 2 are as same as each other, which proves that a convex hull in $[x_{Mn}, x_O, \bar{G}]$ space and the chemical potential diagram $[\mu_{Mn}, \mu_O, \bar{\phi}]$ space is dual to one another.

SI3. Computation of chemical potential diagrams

SI3.1. Linearization assumption

In **Figure S1**, we illustrated the duality between a convex envelope of tangent lines to $U(S)$ and a concave set of points to $F(T)$ for a single phase. To construct a phase diagram, one calculates phase transitions between multiple phases. In the computational DFT community, we often calculate the phase transition boundary between multiple phases as if single phases have infinite curvature in the extensive variables, as shown in **Figure S1b**. For example, if you are calculating temperature-dependent phase transitions using $G(T)$, for each single phase, we linearize $G(T)$, where $G = H - TS$, by treating S as a constant. This linearization assumes a zero curvature for $\partial^2 G / \partial T^2 = C_p/T$; in other words, we are assuming that the heat capacity is zero. Then, each phase is a vertical line in $G(S)$ space, because S is a constant and G is affected by T . A vertical line means the second derivative of thermodynamic potential with respect to S is infinite.

Note that linearizing the thermodynamic potential in intensive variables means that conjugate extensive variables are assumed constant, and the second derivative with respect to intensive variables of a phase is zero. The reflection of this linearization in the conjugated extensive variables is that the second derivatives with respect to them are infinite.

When calculating chemical potential diagrams, we can also linearize $\phi(\mu)$, where $\phi = G - \mu x$, such that x is a constant. Therefore, the second derivative of ϕ with respect to μ is zero. Chemically speaking, a constant x means that we are considering only stoichiometric phases—no off-stoichiometry for a phase is favorable due to a very large energy increase. This linearization assumption also corresponds to the nature of solid-state DFT calculations, since DFT calculations are typically performed on stoichiometric compounds, and it can be laborious to evaluate the energy at off-stoichiometric, disordered compositions.

Linearization produces good approximations of phase boundaries in thermodynamics, and makes calculations faster, while still retaining interpretability. If we truly need to calculate a solution phase, we can include a series of vertices to represent a continuous $G(x)$ curve in the composition axis. Most importantly, linearization also enables the use of computational codes that calculate the half-space intersection. We will discuss this in the following sections.

SI3.2 Computation of chemical potential diagrams through the Intercept Rule

Here, we briefly derive the Intercept Rule in a 2-component system. The affine constraint in a binary space is $x_A = 1 - x_B$. This constraint eliminates a degree-of-freedom, and therefore, a dimension from the chemical space; from G - x_A - x_B to \bar{G} - x_B . Here, $\bar{G} = \mu_A x_A + \mu_B x_B$, so that $d\bar{G} = \mu_A dx_A + \mu_B dx_B$. By substituting the affine relationship of the convex hull where $dx_A = -dx_B$, we can derive: $\bar{G} = \mu_A + (\mu_B - \mu_A) x_B$, $d\bar{G} = (\mu_B - \mu_A) dx_B$. By substituting $(\mu_B - \mu_A)$ with $d\bar{G}/dx_B$, we can get the chemical potential of A or B as: $\mu_B = G(x_B) + (1-x_B)[\partial G(x_B)/dx_B]$, and $\mu_A = G(x_B) - (x_B)[\partial G(x_B)/dx_B]$. Geometrically speaking, this places μ_A and μ_B directly on the \bar{G} -intercepts of the tangent plane to the convex hull where the x_B is either 0 and 1, respectively. The chemical potential then has the same magnitude and units of the formation energy. In other words, the intercept of the tangent line for a phase with the \bar{G} -axis provides the chemical potential of each species in the material at equilibrium.

In **Figure 2** of the manuscript, we use the intercept rule to develop a conceptual understanding of chemical potentials. Additionally, the intercept rule serves as way to demonstrate the duality between the convex hulls and chemical potential diagrams. However, calculation of intercepts require the computation of gradients or normal vectors of phase coexistence regions (tangent planes). This process is computationally expensive when the chemical potential diagram involves more than two components. An alternative, more efficient approach is to calculate the half-space intersection of the convex hull, as it offers greater ease of scalability to higher dimensions.

SI3.3. Computation of chemical potential diagrams through half-space intersection

SI3.3.1. Phase diagram with all chemical potential axes

Half-space intersections offer an easy and scalable approach to construct chemical potential diagrams. First, we define the grand potential for each phase using $\phi = G - \sum \mu_i x_i$, then we construct a half-space intersection. The implementation python codes and tutorial examples are in Github link:

https://github.com/dd-debug/chemical_potential_diagram_and_convex_hull_and_pourbaix_diagram

We utilize the *HalfspaceIntersection* class from *scipy* to get the dual of points from each single phase from the convex hull. To use the *HalfspaceIntersection*, we need to prepare the coefficients in a form of $AX + B \leq 0$, where A and B are each a coefficients matrix, and x is variables matrix. **Eq. S3** shows the corresponding matrix form in our study. Each single phase corresponds to one row of A and B coefficient matrix, formed by composition x_i and formation energy G . Each row defines a hyperplane in the ϕ - μ_i space. This is why the Linearization assumption is necessary, because it ensures each single phase has stoichiometric composition to fulfill the input requirements of *HalfspaceIntersection* class.

Therefore, each phase is a flat hyperplane in ϕ - μ space. All these hyperplanes then form a half-space intersection – which produces a lower inner envelope, which produces whatever phase has the lowest free energy ϕ at a specific set of applied chemical potentials.

$$AX + B \leq 0$$

$$\begin{bmatrix} (x_1 & x_2 & \dots & x_N & 1)_\alpha \\ (x_1 & x_2 & \dots & x_N & 1)_\beta \\ \dots \end{bmatrix} \begin{bmatrix} \mu_1 \\ \mu_2 \\ \dots \\ \mu_N \\ \phi \end{bmatrix} + \begin{bmatrix} -G_\alpha \\ -G_\beta \\ \dots \end{bmatrix} \leq 0 \quad \text{Eq. S3}$$

HalfspaceIntersection constructs a fully enclosed polytope, and so we also need border hyperplanes and an internal point to define the region to enclose by half-space intersection. Border hyperplanes are constructed based on the boundary limits of the chemical potential as we choose, which ensures that the half-space is enclosed. Then, the half-space intersection can be calculated. Next, using the *intersection* attribute from the *HalfspaceIntersection* class, we obtain the domain information of single-phase and phase-coexistence regions, and chemical potential diagrams are ready to plot.

SI3.3.2. Equilibrium Envelope

The chemical potential diagrams generated in this study include scenarios of both equilibrium and non-equilibrium conditions, as shown in manuscript **Figure 2c, d**. To the best of our knowledge, this is the first time that this complete chemical potential diagram is reported, which also shows the growth and dissolution chemical potential ranges of each phase. Existing chemical potential diagrams in the literature are exclusively confined to equilibrium conditions, constituting a specific subset of the complete chemical potential diagram, where $\phi = [G]_{internal} - [\sum_i \mu_i x_i]_{external} = 0$, signifying the equivalence of external applied chemical potential to the internal chemical potential at equilibrium. We called this equilibrium version of chemical potential diagram as the *equilibrium envelope*.

Following the same procedure, we can also use *halfspaceintersection* Class to construct the equilibrium envelope, by removing ϕ variable and its coefficient, because $\phi = 0$. This can be expressed as:

$$AX + B \leq 0$$

$$\begin{bmatrix} (x_1 & x_2 & \dots & x_N)_\alpha \\ (x_1 & x_2 & \dots & x_N)_\beta \\ \dots \end{bmatrix} \begin{bmatrix} \mu_1 \\ \mu_2 \\ \dots \\ \mu_N \end{bmatrix} + \begin{bmatrix} -G_\alpha \\ -G_\beta \\ \dots \end{bmatrix} \leq 0 \quad \text{Eq. S4}$$

SI4. Computation of mixed composition/chemical potential diagrams

We now describe the computational construction of mixed composition and chemical potential diagrams. The implementation Python codes and tutorial examples are in Github link:

https://github.com/dd-debug/chemical_potential_diagram_and_convex_hull_and_pourbaix_diagram

Our approach here involves the extraction of extensive variables x_i information from the convex hull, followed by the acquisition of intensive variables μ_i from chemical potential diagrams. Note that all the compositional data of both single-phase and phase coexistence regions are embedded in the Pymatgen convex hull phase diagram analysis package. Furthermore, the computation of chemical potential information can be achieved through our half-space intersection (**SI3.3**) method.

This approach also facilitates our comprehension of the relationship between dimensionality and the number of coexisting phases in different kinds of mixed μ - x diagrams, a topic discussed in the Part I of these three-part series of high dimensional phase diagram papers.

Our discussion focuses on the equilibrium states of materials, with chemical potential information derived from the equilibrium envelope (outlined in section **SI3.3.2**) from the chemical potential diagram. Using a ternary system as an example, in compositional space (x_1 - x_2 - x_3), each single phase is represented as a point, a 2-phase coexistence is symbolized by a tie line connecting the two single phases, and a 3-phase coexistence is a triangular region defined by three single phases as terminal points. In contrast, when considering a ternary system in chemical potential space (μ_1 - μ_2 - μ_3), each single phase is characterized as a 2D polygon, and a 2-phase coexistence region is a linear segment shared by two single phases. In this scenario, a 3-phase coexistence region simplifies to a point, as no degree of freedom exists for chemical potential alterations at such a juncture. This point corresponds to the intercepts of a tangent plane over a 3-phase coexistence triangle on the convex hull.

SI4.1. μ_1 - μ_2 - x_3 phase diagram (x_{Ta} - μ_0 - μ_N)

Within the μ_1 - μ_2 - x_3 phase diagram, the dimensionality of a single phase depends on the projection of the equilibrium envelope onto the μ_1 and μ_2 axes. Each material is inherently represented as a 2-D polygon within the μ_1 - μ_2 - μ_3 space, which implies that its projection onto any two μ_1 and μ_2 axes generally results in 2-D polygons. However, when we project a 2-D polygon from the 3-D (μ_1 - μ_2 - μ_3) space onto a 2-D (μ_1 - μ_2) plane, the information related to μ_3 is disregarded. The dimensionality of this projection hinges on the orientation of the plane in the 3-D space. For instance, as illustrated in **Figure 3c**, if we had phases without Ta, they would be lines when projected to μ_0 and μ_N (here we manually remove all N_xO_y gas phases); whilst phases with Ta are 2-D polygons. Further discussion regarding this projection methodology can be found in Part III of this 3-part series.

A 2-phase region is a 1D line in both a ternary convex hull and ternary chemical potential diagram, so it is 2D rectangle in μ_1 - μ_2 - x_3 diagram that has one principal axis in the μ_1 - μ_2 plane, and one principal axis in the x_3 direction. A 3-phase coexistence has a fixed chemical potential μ_1 , so it is a vertical line parallel to the x_3 direction. To identify 2-phase or 3-phase regions, we systematically examine every combination of two / three single phases to see if they shared a common line / vertex. Finally, 2-phase regions are plotted as vertical plane, and 3-phase regions are plotted as vertical red lines, as shown in manuscript **Figure 3b**.

SI4.1. μ_1 - x_2x_3 phase diagram (μ_{Li} - x_{Mn} - x_{O})

Because of the affine constraint, the molar ratio between Element 2 and Element 3 can be represented with a single variable, which we refer to as x_2x_3 . This means that a μ_1 - x_2x_3 phase diagram is in fact a 2D phase diagram. A single phase on the equilibrium envelope of a μ_1 - μ_2 - μ_3 diagram is given by a 2-D polygon, meaning it has a single value of x_2x_3 ; and a linear μ_1 range for the single phase, defined by calculating its maximum and minimum values along the μ_1 axis. As a result, a single phase is depicted as a 1-D line parallel to the μ_1 axis, as shown in manuscript **Figure 4d, e, f**.

A 2-phase region appears as a line in both the ternary convex hull and the three-component equilibrium envelope. This implies that a 2-phase region in μ_1 - x_2x_3 diagram is a 2D rectangle. During the calculation of the equilibrium envelope, the *HalfspaceIntersection* class returns facets in the form of interconnected triangles, collectively forming two-dimensional polygons corresponding to individual phases. Co-planar triangles may need to be merged in order to produce non-simplicial polygons. The identification of the boundary lines for each phase can be achieved by counting the number of appearances for each boundary line. Specifically, the true boundary lines associated with a single phase occur only once, whereas interior edges formed from two co-planar triangles are counted twice, since they share two adjacent triangles.

To find the μ_1 range of 2-phase regions, we systematically examine every combination of two single phases to see if they share common boundary lines. If they do, it represents the two phases can coexist. This process yields the μ_1 span for each 2-phase coexistence region, which can be combined with the calculation of the two-phase coexistence regions for x_2x_3 from a convex hull to generate a 2D rectangle.

Since a 3-phase region is characterized by a single point, with fixed chemical potential values, its dimensionality depends on the projection of a 3-phase triangle from convex hull to x_2x_3 space, resulting in a 1D line that is parallel to the x_2x_3 axis. Similar to the approach used for 2-phase regions within equilibrium envelope, we systematically examine every combination of three single phases to see if they shared a common vertex. If they do, it signifies a 3-phase coexistence region. By finding its μ_1 value and calculating the molar ratio x_2x_3 range of the three coexisting phases, a horizontal 3-phase line could be constructed, as shown as the horizontal red line in manuscript **Figure 4d, e, f**.

SI4.3. μ_1 - x_2 - x_3 - x_4 phase diagram (μ_{O} - x_{Ni} - x_{Cr} - x_{Co})

Quaternary systems follow a similar pattern as ternary systems. In convex hulls, a 4-phase coexistence region is a 3D tetrahedron. Unlike the convex hull, the equilibrium envelope does not use barycentric coordinates, necessitating a discussion on the visualization of higher dimensional polytopes. Intuitively, the μ_1 - x_2 - x_3 - x_4 diagram can be envisioned as a compilation of various ternary Gibbs compositional triangles x_2 - x_3 - x_4 at different μ values. In the μ -axis, single phase regions are vertical lines since they have fixed composition and linear range on μ_1 axis. By determining the maximum and minimum values of μ_1 for each phase, we can visualize single phases. All the single, 2-phase, and 3-phase coexistence regions within a ternary composition phase diagram are preserved. The interesting coexistence phenomena in a μ_1 - x_2 - x_3 - x_4 then arise at the boundaries between ternary phase diagram slices, as discussed below.

For a 2-phase region, the chemical potential can change along μ_1 . So, a 2-phase region can be a vertical rectangle connecting two single phase vertical lines (here vertical refers to parallel to the μ axis). 2-phase coexistence can also represent the crossover point between two pure phases in the vertical axis, for example, the point between Co and CoO.

Given that the exhaustive combination of every two single phases in a 4-component system can be computationally demanding, we adopt an efficient approach. Initially, we identify the distinct μ_1 ranges shared by different sets of entries. Subsequently, we extend the compound phase diagram along the μ_1 direction, generating triangular prisms for each specific μ_1 range. Finally, these triangular prisms are interconnected to form a comprehensive representation. This method leverages the *GrandPotentialPhaseDiagram* class from pymatgen to construct the compound phase diagram.

In the case of a 3-phase region, besides one degree of freedom offered by chemical potentials, the 3-phase triangle within the convex hull can be transformed into a $x_2x_3x_4$ Gibbs triangle. In this scenario, the overall dimensionality is 3-D. To be more specific, the 3-phase region takes the form of a triangular prism, with the Gibbs triangle extending along the μ_1 direction. As discussed in the manuscript, a 4-phase region assumes the shape of a Gibbs $x_2x_3x_4$ triangle. This is because the chemical potentials are fixed (resulting in 0-D), while the composition is allowed to vary within the $x_2x_3x_4$ triangle.

SI5. A generalized phase rule for mixed μ - x diagrams

Here we detail a generalized phase rule for the dimensionality of phase coexistence regions in mixed μ - x phase diagrams. In a system with N components, these regions possess $N - C$ dimensions in chemical potential space and $C - 1$ dimensions in convex hull space, based on Point-line duality. When all elements of the C-phase span all composition axis, the dimensionality remains $N - C$, if the number of μ -axes (N_μ) used for visualization is more than $N - C$. For instance, a 2-phase region in a quaternary system within μ_1 - μ_2 - μ_3 space is 2-D. However, if N_μ is smaller than $N - C$, the dimensionality of the C-phase coexistence regions is reduced to N_μ .

N : elements number

N_μ : the number of μ axis to be visualized

$N - C$: dimensionality of a C-phase coexistence region in μ space.

For μ , dimensionality of a C-phase coexistence region to be visualized is: $\min(N - C, N_\mu)$

Similarly, if the number of composition axis we want to visualize (N_x) is smaller than the dimension number of C-phase coexistence region ($C - 1$), for the visualization of composition axis, the C-phases coexistence polytope dimensions are N_x .

N_x : the number of x axis to be visualized

$C - 1$: dimension of a C-phases coexistence region in compositions space

For x , dimensionality of a C-phase coexistence region to be visualized is: $\min(C - 1, N_x - 1)$

Finally, we add the dimensions for μ and composition together.

Finally, the dimensionality of a C-phase coexistence polytope for a N -component system in a μ - N_μ - x - N_x diagram is: $\min(N - C, N_\mu) + \min(C - 1, N_x - 1)$

For example, for 1-phase region for quaternary system in μ_1 - μ_2 - x_3x_4 phase diagram, for μ , dimension to be visualized is $\min(4 - 1, 2)$ D, which is 2D; for compositions, dimension to be visualized is $\min(2 - 1, 2 - 1)$, which is 1D. Therefore, the total dimension is 3D. We also offer other quaternary system dimensionality of phase coexistence regions in **Table S2**.

Table S2. Table of dimensionality of phase coexistence regions in quaternary μ - x phase diagrams.

	1-phase	2-phase	3-phase	4-phase
μ_1 - μ_2 - μ_3 - μ_4	3-D polytope	2-D plane	1-D line	0-D point
x_1 - x_2 - x_3 - x_4	0-D point	1-D line	2-D triangle	3-D tetrahedron
μ_1 - x_2 - x_3 - x_4	1-D line	2-D vertical rectangle	3-D triangular prism	2-D triangle
μ_1 - μ_2 - μ_3 - x_4	2-D polygons for phases w/o x_4 ; Others: 3-D polytopes	2-D rectangle for 2-phase w/o x_4 ; 3-D prism for others;	1-D line for 3-phase w/o x_4 ; 2-D rectangle for others	1-D line
μ_1 - μ_2 - x_3 - x_4	1-D lines for phases w/o x_3 & x_4 ; Others: 2-D polygons	If x_4 is covered in 2-phase: 3-D polytope	If x_4 is covered in 3-phase: 2-D polygon	1-D line